

Uncertainty Estimation Based On Global Sensitivity Analysis For CFD Simulations Of Supersonic Flow Over Missile

Kadu Pravin Ananta

A Thesis Submitted to
Indian Institute of Technology Hyderabad
In Partial Fulfillment of the Requirements for
The Degree of Master of Technology



भारतीय प्रौद्योगिकी संस्थान हैदराबाद
Indian Institute of Technology Hyderabad

Department of Mechanical and Aerospace Engineering

June 2016

Declaration

I declare that this written submission represents my ideas in my own words, and where ideas or words of others have been included, I have adequately cited and referenced the original sources. I also declare that I have adhered to all principles of academic honesty and integrity and have not misrepresented or fabricated or falsified any idea/data/fact/source in my submission. I understand that any violation of the above will be a cause for disciplinary action by the Institute and can also evoke penal action from the sources that have thus not been properly cited, or from whom proper permission has not been taken when needed.

Pakadu

(Signature)

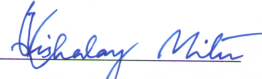
(Kadu Pravin Ananta)

ME14MTECH11007

(Roll No.)

Approval Sheet

This thesis entitled "Uncertainty Estimation Based On Global Sensitivity Analysis For CFD Simulations Of Supersonic Flow Over Missile" by Kadu Pravin Ananta is approved for the degree of Master of Technology from IIT Hyderabad.



Dr. Kishalay Mitra

(Examiner)



Dr. Karri Badarinath

(Examiner)



Dr. Raja Banerjee

(Adviser)

Acknowledgements

I would first like to thank my thesis advisor Dr. Raja Banerjee of the Department of Mechanical and Aerospace Engineering at IIT Hyderabad. He has been supportive since the days I began working on my research work. He consistently encouraged and allowed this research to be my own work, but steered me in the right direction whenever he thought I needed it. One simply could not wish for a better or a friendlier advisor.

I am thankful to Sumit Jadhav for his help while commencing my thesis work. I am indebted to Nikhil Kalkote, Vatsalya Sharma and Ashwani Assam. They have supported me in a number of ways including technical advice and answers to many queries.

I must express my very profound gratitude to my friends: Rakesh Kale, Anil Wakale, Mahendra Date, Prasad Kangude and Samadhan Patil.

Finally, I would like to thank my family, who have supported me unconditionally throughout my whole life and education – none of this would not have been possible without them.

Dedication

To my parents and beloved ones...

Abstract

Though Computational Fluid Dynamics (CFD) approach has proven itself as a cost-effective in designing of missiles, CFD simulations cannot accurately estimate the experimental data due to such reasons as unphysical sub-models, insufficient resolution, inaccurate boundary conditions, and initial conditions, etc. To account the uncertainty due to such sources, Global Sensitivity Analysis (GSA) approach is proposed in the current work of supersonic flow over cruciform missile of ogive-cylinder fuselage-wings-fins configuration. The output parameters of interest considered are the coefficient of rolling moment, the coefficient of drag, and coefficient of lift. A grid convergence study is done to check grid independence and Grid Convergence Index (GCI) for these global coefficients, and local mach number and stagnation pressure change field variables are estimated. A nominal case is established. Global Sensitivity Analysis is performed by perturbation of the parameters from their nominal case value after identifying the sources of uncertainty and the input variables with greater influence on output global parameters are identified.

Contents

Declaration	ii
Approval Sheet	iv
Acknowledgements	v
Abstract	vii
Contents	viii
Abbreviations	x
List of Symbols	xi
List of Figures	xiii
List of Tables	xiv
1 Introduction	1
1.1 Motivation	1
1.2 Introduction To Uncertainty	1
1.2.1 Uncertainty due to modelling	2
1.2.2 Uncertainty due to numerical error	3
1.3 Importance Of Sensitivity Analysis	4
1.4 Thesis Outline	4
2 Literature Review	5
2.1 Approach For Sensitivity Analysis	5
2.2 External Flow Over Missile	6
2.3 Identifying The Sources of Uncertainty	6
3 Problem Specifications	8
3.1 Background	8
3.2 Forces and Rolling Moment	10
3.2.1 Drag and Lift Forces	10
3.2.2 Rolling Moment	12
3.3 Coefficients	12
3.4 Geometrical Elucidation	13
3.5 Problem Definition	14
3.6 Essentials	15

4	GCI And Identification Of Uncertainty Sources	16
4.1	Grid Independence Study	16
4.1.1	Richardson Extrapolation	16
4.1.2	Grid Convergence Index	18
4.1.3	Steps to Calculate GCI	18
4.2	Geometrical Sensitivity	19
4.3	Turbulence Modelling	19
4.3.1	RANS and Boussinesq Approximation	20
4.3.2	Spalart Allmaras Model	21
4.3.3	Standard $k - \omega$ Model	22
4.3.4	SST $k - \omega$ Model	22
4.3.5	Turbulent Intensity	23
4.4	Viscosity Model	23
4.4.1	Sutherland's Law	24
4.4.2	Viscosity Modelling Using Kinetic Theory	24
4.4.3	Power-Law Viscosity Model	24
4.5	Thermal Conductivity Model	24
4.5.1	Thermal Conductivity Modelling Using Kinetic Theory	25
4.5.2	Thermal Conductivity Using Polynomial Of Temperature	25
4.6	Specific Heat	25
4.6.1	Specific Heat Using Kinetic Theory	26
4.6.2	Piecewise Polynomial	26
4.7	Static Temperature Sensitivity	26
4.8	Convective Flux Type	27
4.9	Order of Discretization Scheme	27
4.10	GSA Parameters	27
5	Nominal Case	29
5.1	Mesh Generation	29
5.2	Solver Settings	31
5.3	Nominal Case Results	32
5.3.1	Values of Coefficients	32
5.3.2	Contour Plots	34
5.3.3	Comparison of Contours	37
6	GCI And GSA Results	41
6.1	GCI Results	41
6.1.1	GCI For Global Output Parameters	41
6.1.2	GCI For Local Field Variables	42
6.2	GSA Results	46
7	Conclusions and Future Scope	49
	References	50

Abbreviations

GSA	Global Sensitivity Analysis
GCI	Grid Convergence Index
GSA	Global Sensitivity Analysis
GCI	Grid Convergence Index
PDEs	Partial Differential Equations
RE	Richardson Extrapolation SA Spalart Allmaras
$k - \omega$ SST	$k - \omega$ Shear Stress Transport
RSM	Reynolds Stress Model
TI	Turbulence Intensity
Roe-FDS	Roe Flux-Differencing Splitting Scheme
AUSM	Advection Upstream Splitting Method
MUSCL	Monotonic Upstream-Centered Scheme for Conservation Laws

List of Symbols

T	True value
S	Simulation result value
ξ	Error
U_S	Simulation uncertainty
D	Diameter of fuselage (cm)
α	Angle of attack (degree)
ϕ	Roll angle (degree)
z	Wing distance from nose tip (cm)
M	Mach number
P_T	Stagnation pressure (Pa)
T_T	Stagnation temperature (K)
P	Static pressure (Pa)
T	Static temperature (K)
u	Velocity (m/s)
C_m	Coefficient of rolling moment
C_D	Coefficient of drag
C_L	Coefficient of lift
F_D	Drag force
F_L	Lift force
F_A	Axial force
F_N	Normal force
\vec{F}_P	Pressure force vector
\vec{F}_V	Viscous force vector
\vec{M}	Rolling moment
\vec{a}	Specified directional vector
\vec{r}_o	Radial vector from central axis
$d\vec{A}$	Elemental surface area
τ	Shear stress
Re	Reynolds number
A	Cross-sectional area
μ	Dynamic viscosity (Pa·s)
ν	Kinematic viscosity (m ² /s)
u^+	Dimensionless velocity
y^+	Dimensionless wall distance

Pr	Prandtl number
u_τ	Shear velocity
ψ	Output variable
h	Representative grid size
n	Apparent order of accuracy of method
r	Refinement factor
N	Total number of nodes
k	Turbulence kinetic energy
ω	Specific dissipation rate
I	Turbulent Intensity

List of Figures

3.1	Tactical Missile Configurations	9
3.2	Types of Missile: (a) Cruciform Missile, (b) Planform Missile	9
3.3	Angles Representation: (a) Angle of Attack, (b) Roll Angle	10
3.4	Forces Resolution	11
3.5	Geometrical Representation: (a) Missile Body Dimensions, (b) Wing Dimensions, and (c) Fin Dimensions	13
3.6	Missile Geometry	14
4.1	Geometrical Sensitivity	19
4.2	Thermal Conductivity as the Function of Temperature	25
5.1	Missile with Computational Domain	29
5.2	Meshing of Missile Body	30
5.3	Meshing of Computational Domain	31
5.4	Convergence of C_m , C_D and C_L	33
5.5	Mach Number Contours at Plane $Y = 0$	34
5.6	Prandtl-Meyer Expansion and Bow Shock at Plane $Y = 0$	34
5.7	Mach Number Contours at Plane $Z = 0$	35
5.8	Bow Shock at Plane $Z = 0$	36
5.9	Circulation and Reattachment at Plane $Z = 0$	36
5.10	Sectional Contours Of Normalized Stagnation Pressure Change	37
5.11	Contours Comparison of Pressure Change at Planes $X = 4D$, $7.5D$, $10D$	38
5.12	Contours Comparison of Pressure Change at Planes $X = 11D$, $13D$, $15D$	39
5.13	Plot for Comparison of Pressure Change Contours at Plane $7.5D$ and $R = 30$ cm	40
6.1	Line Drawn In Space To Evaluate Local GCI	42
6.2	Local GCI Evaluation For Mach Number On Specified Line	45
6.3	Local GCI Evaluation For Normalized Stagnation Pressure Change On Specified Line	45
6.4	GSA For C_m	47
6.5	GSA For C_D	47
6.6	GSA For C_L	48

List of Tables

1.1	Sources of Uncertainty [1]	3
3.1	Boundary Conditions	14
4.1	GSA Parameters	28
5.1	Nominal Case Result for Coefficients	33
6.1	GCI Estimation For Global Output Parameters	42
6.2	GCI For Local Mach Number Over A Specified Line	43
6.3	GCI For Local Pressure Change Over A Specified Line	44
6.4	GSA Results	46

Chapter 1

Introduction

1.1 Motivation

Computational fluid dynamics (CFD) is increasingly being used for conceptual studies of product design, and detailed product development. Its application throughout the evolution of advanced tactical missiles is also notable. Role of CFD in development of a missile is explained by Frostbutter et al. [2]. From starting of a missile development program to the final stage of integrating missile into fleet, the process undergoes through many steps such as evaluation of alternate airframe, performing wind tunnel tests, developing subsystems and hardware, and performing flight tests. CFD is used to perform aerodynamic coefficient trade studies in the stage of airframe designing for the primary observation by reducing cost of instrumentation. CFD does not eliminate the usage of wind tunnel testing but instead provides supplementary test results which can be invaluable in all phases of wind tunnel testing. For example, inviscid solution of CFD can be used to predict the pressure and temperature distribution which is supportive for selection and location of instrument. Recent CFD developments in multi-zone structured, unstructured, and adaptive grid refinement, complemented by multiprocessor algorithms, have boosted the speed of simulations and hence reduced the time required to obtain results. Agbaglah et al. [3] has demonstrated the reduction in time due to parallelization and adaptive grid refinement with the example of the droplet simulation. The requirement of missiles for higher speed, greater manoeuvrability, and superior functionality in different conditions with a reduced amount of designing time is also a reason for increase in demand of CFD. Though CFD approach has proven itself as a cost-effective in designing of missiles, CFD simulations cannot accurately estimate the experimental data due to such reasons as unphysical sub-models, insufficient resolution, inaccurate boundary conditions, and initial conditions, etc. These sources which can be divided into modelling and numerical in nature constitute to uncertainty in solution. Thus, it is necessary to investigate these uncertainties.

1.2 Introduction To Uncertainty

Uncertainty is defined by ASME [4] as an inherent property of measurement technique or model description and is due to lack of knowledge while the error is defined as the difference between the exact value to a problem and the answer computed from a faulty method or simplified theory. This

implies that the uncertainty is of probabilistic nature and error as deterministic nature. Though there is the difference between uncertainty and error natures, we have used a more general definition of uncertainty that includes error where they cannot be distinguished. The sources of uncertainty and error are broadly categorized by Oberkampf et al. [1] into two distinct parts: (i) modelling uncertainty and (ii) numerical uncertainty.

1.2.1 Uncertainty due to modelling

Modelling uncertainty arises due to the assumptions made in representing a particular physical phenomenon in mathematical form, auxiliary physical models, and boundary conditions.

Sometimes assumptions are made such as continuum fluid, inviscid flow, incompressible flow, etc. for the sake of simplicity. Fluids made up of discrete molecules are considered to be continuous, and the assumption is coined as continuum hypothesis. Continuum hypothesis can introduce error in cases of small scales and extremely high altitude applications. Low viscosity fluids can be assumed to be inviscid; this may lead to the disagreement in actual value and result from inviscid solution. Distinguishing term between compressible and incompressible flow is Mach number. Density is considered to be constant in both space and time when Mach number is less than 0.3 which is corresponding to 5% change in density. Incompressible flow assumption enables the decoupling of energy equation with Navier-Stokes equations and continuity equation for CFD solution method, and this results in a saving of computational efforts. But every time this assumption may not be true. For example, water hammering is a phenomenon where compressibility effect on water is evident due to the high pressure that is exerted on it. Near wall treatments of wall-bounded turbulent flows and Boussinesq eddy viscosity assumption are also the sources of uncertainty in case of turbulent flows.

The compressibility factor which is the ratio of the molar volume of a gas to the molar volume of an ideal gas at the same temperature may deviate from unity due to the larger pressure and the lower temperature. Thus to measure density, different equations of state can be used by considering their individual advantages. Thermodynamic properties such as specific heat, thermal conductivity, etc. may not be constant and their values may change with the change in temperature and pressure. Different representative equations are available to consider effects of temperature and pressure on such transport properties.

Boundary conditions such as wall roughness, far-field condition, pressure inlet, velocity inlet as well as geometric representation of the boundaries are also the potential sources of uncertainty. Wall-roughness affects boundary layer region of wall-bounded turbulent flows and it hence ultimately affects the drag and heat and mass transfer on the walls. Examples are the flows over an airfoil, ships, missiles, turbo-machinery, etc. Inlet boundary conditions subjected to error due to an error in measurement techniques used. In the case of geometry, minute details of complex geometry is usually ignored due to difficulty in modelling, and meshing such geometric features and also due to non-availability of adequate computational resources. One can simplify three-dimensional geometry into a two-dimensional geometry. Welding burr and small grooves can be ignored while creating geometry. But these burrs and grooves can affect the boundary layer development and sometimes can cause a considerable disagreement between experimental and computational data.

1.2.2 Uncertainty due to numerical error

The numerical errors arises due to the numerical approach used in solving these mathematical equations. A numerical approach used in solving Navier-Stokes equations, continuity equation and energy equation is still under constant development. Different discretization schemes have been proposed and each of these schemes has their own advantages and disadvantages such as divergence issues, accuracy, and implementation problems. The importance of discretization error diminishes with grid refinement. Again, convergence criterion can be of different types. It can be residual convergence, coefficients convergence or total time. This also can produce uncertainty in solution.

Limited computational resources can influence the use of precision arithmetic. But for some problems incorporating multiphase models, high thermal conductivity ratio, diverse length scales; it is essential to use double precision solver and will be inappropriate if single precision solver used.

These uncertainty sources are tabulated as in Table (1.1).

Table 1.1: Sources of Uncertainty [1]

Sources		Example
Modelling	Physical Modelling (assumptions in PDEs)	Continuum assumption Inviscid flow, Viscous flow Incompressible flow Transitional / Turbulent flow
	Auxiliary Physical Models	Equation of state Thermodynamic properties Transport properties Chemical models, reactions and reaction rates
	Boundary Conditions	Wall, e.g. roughness, Open, e.g. far-field Inlet conditions, e.g. pressure, temperature, mach number Geometrical representation
Numerical	Discretization and Solution	Truncation error – spatial and temporal terms Convergence criterion
	Round-off Error	Finite – precision arithmetic

Simulation error (ξ_S) defined by Stern and Wilson et al. [5] is nothing but a difference between the simulation result value (S) and the true value (T). Simulation error can be calculated by summing

up modelling simulation error (ξ_{SM}) and numerical simulation error (ξ_{SN}).

$$\xi_S = S - T = \xi_{SM} + \xi_{SN} \quad (1.1)$$

Simulation uncertainty (U_S) can be postulated in terms of modelling uncertainty (U_{SM}) and numerical uncertainty (U_{SN}) as in equation (1.2):

$$U_S^2 = U_{SM}^2 + U_{SN}^2 \quad (1.2)$$

From a design point of view, determining these uncertainties for the flow and or thermal simulations are of prime importance. To determine the uncertainty, it is essential to identify the parameters which affect the solution predominantly, and this can be done by Sensitivity Analysis.

1.3 Importance Of Sensitivity Analysis

One of the primary reason of increased interest in uncertainty management is its application in risk-based design methods. As CFD is being widely used in aerospace industries, uncertainty has been seen as an important research area. But to carry out the uncertainty analysis using methods, like Monte Carlo simulations with a large number of sample points, is computationally expensive and therefore not practical. Sensitivity analysis comes to rescue at this point in which extreme condition approach is used here. Sensitivity analysis gives the insight to identify the set of parameters which would be having a considerable effect on the result. Furthermore, these parameters can be used for investigating the interdependency amongst them and for the total uncertainty. Parameters which have marginal influence on the overall design objective can be dropped from further analysis. This helps in part to mitigate computational cost.

1.4 Thesis Outline

- Chapter 2 details about the literature review done for the global sensitivity analysis, grid convergence index, missile body simulation and the sources of uncertainty.
- Chapter 3 explains the missile dimensions, output quantities of interest and boundary conditions.
- Chapter 4 discusses the sources of uncertainty in detail.
- Chapter 5 represents the nominal case results.
- Chapter 6 reports the grid convergence index and global sensitivity analysis.

Chapter 2

Literature Review

The literature survey includes the understanding of the approach solving for sensitivity analysis, of external flow over missile simulation, and identification of possible sources of uncertainty.

2.1 Approach For Sensitivity Analysis

A number of approaches to uncertainty and sensitivity analysis have been developed, including differential analysis in which linear approximation - a partial derivative of flow with respect to parameters has been incorporated in Ref. [6] [7] [8]. For simulation-based design, Du and Chen [9] use two approaches, namely, the extreme condition approach and the statistical approach, which are developed to propagate the effect of uncertainties across a design system comprising interrelated subsystem analysis. Using the extreme condition approach, an interval of the output from a series of simulations is obtained, while the statistical approach provides statistical estimates of the output. Local sensitivity analysis involves the local perturbation of model constants or variables and is computationally expensive while Global Sensitivity Analysis (GSA) can be used for uncertainty in the boundary conditions, models, model constants and other numerical parameters. GSA is carried out by Pei et al. [10] for a diesel engine simulation to study the sensitivities of various modelling constants and boundary conditions in a global manner in which the output results such as liquid penetration length, ignition delays, combustion phasing, and emissions are intended. The experimental uncertainty of wind tunnel experimentation is described by Rhode et al. [11] in which a range of sources are considered such as measuring instrumental error, instrumentation asymmetries, and flow-field non-uniformity and uncertainty calculated in this is with a baseline configuration. Uncertainty is reported in terms of residual and sample variance. Residual is defined as the absolute value resulted from the pressure coefficient of a performed experiment minus its average value calculated from total performed experiments. Sample variance is then calculated from the residuals.

Celik et al. [12] have summarized the Grid Convergence Index (GCI) method which can be applied to check grid independence. The method involves performing the simulation on three successively finer grids and defining the error percentage on one of the grid. This extracted study of GCI is thoroughly explained by Celik et al. [13]. Richardson Extrapolation (RE) is used to establish a method for grid independent solution with the example of backward facing step. A similar approach is explained by Luis Eça [14] in which a procedure is presented for the numerical uncertainty

in numerical approach for which exact solution is undetermined. This procedure is proposed by considering the limitation in grid refinement. An attempt of grid independence check is done by Abdol-Hamid et al. [15] for Ares I class of vehicle which is a two-stage rocket. Error estimation for aerodynamic characteristics derived from iterative convergence grid refinement is presented in it.

In the present study, the extreme condition approach is implemented for GSA by avoiding interdependence of parameters which may not be true in real. The parameters are perturbed from base case value and their effects are observed on the targeted values. This GSA works as a selection method to highlight those parameters whose correctness and adjustments are most probable to influence the predictions of a computational model.

2.2 External Flow Over Missile

GSA is carried out for supersonic flow a missile body. Khelil et al. [16] reported the numerical evaluation of roll induced moment for a cruciform tactical missile, and the results are compared with experimental data. Two configurations of the missile are considered which are a fuselage with four fins and a fuselage with four fins, and four wings. Results are presented for different angle of attacks, roll angles and mach numbers. The geometry of the missile has been taken from this literature. A set of the input parameters from this work is considered in the present study of sensitivity analysis.

2.3 Identifying The Sources of Uncertainty

Identification of key parameters which would be possible sources of uncertainty is of prime importance. A number of separate literature are available which contains the effects of the different parameters. An overview of the sources of uncertainty for CFD is propounded by Oberkampf [1]. The sources include the parametric uncertainty and physio-chemical modelling uncertainty.

While performing CFD simulations with turbulence modelling for practical engineering geometries, Reynolds Averaged Navier Stokes (RANS) based turbulence models are typically used. Several RANS based turbulence models have been proposed which can be classified into multiple genres: one-equation model, two-equation models, and Reynolds Stress Model can be used. Spalart and Allmaras [17] have elucidated a model called Spalart Allmaras (SA) model which is one-equation model. SA model has been used effectively for compressible flow conditions [18] [19]. Standard $k - \omega$ model was proposed by Wilcox [20] which is a two-equation model. Menter [21] introduced $k - \omega$ Shear Stress Transport ($k - \omega$ SST) model which is the modified version of standard $k - \omega$ model and accounts for adverse pressure gradients effectively. Both models were compared by Coussirat et al. [22]. These models consider the turbulent viscosity as isotropic and it leads to inaccurate computation of rolling moment. Launder et al. [23] proposed Reynolds Stress Model (RSM) that helps to capture anisotropic nature of the flow. Turbulence Intensity (TI) which is used to quantify the turbulence in flow also affects the flow solution and effect of TI has been demonstrated by Shao-wu LI et al. [24] for the airfoil flow simulation.

For fluid material which is air, in this case, transport properties like density calculation from an equation of state, specific heat and viscosity are the possible parameters that can effect the solution accuracy. Different physical models are developed for these properties. Redlich-Kwong Real Gas

introduced by Redlich et al. [25] and Peng-Robinson equation of state stated by Peng et al. [26] can be used in addition to ideal gas law equation of state. Molecular viscosity plays a key role while solving for wall bounded flow and when drag force is considered. Sutherland's law [27] along with kinetic theory based viscosity models are suitable which are presented using the function of temperature. Stephan et al. [28] has presented the model for the change in thermal conductivity with respect to temperature and pressure. Thermal conductivity is articulated in terms of pressure and temperature and polynomials are given for different ranges of pressure and temperature.

Rhode et al. [11] have performed various simulations considering uncertainty in measurements in mach number, pressure, total temperature, and angles. It is done by introducing an error bound of the measurement technique. The error in the measurement can be distinct for different types of measurement techniques. Boundary conditions required for CFD solver can undergo uncertainty and it has been explained through the experimental setup of a wind tunnel.

Numerical uncertainty can be due to convective flux type and discretization schemes used while formulating the set of discretized equations. Convective fluxes can be computed by Roe Flux-Differencing Splitting Scheme (Roe-FDS) proposed by Roe [29] and Advection Upstream Splitting Method (AUSM) proposed by Liou et al. [30] with the applications in supersonic flow over NACA airfoil and cylinder. Both methods are compared by Roe [29] and Lee et al. [31] which explains that AUSM is superior to Roe-FDS in terms of convergence and bow shock but still introduces numerical oscillations and pressure overshoots after the strong normal shock. Discretization schemes can be of first order or second order or a hybrid scheme. Advantages of Monotonic Upstream-Centered Scheme for Conservation Laws (MUSCL) is explained by Anderson et al. [32].

Chapter 3

Problem Specifications

3.1 Background

A tactical missile comprises of many integrants such as airframe, propulsion system, flight control system, guidance system, etc. From an aerodynamics point of view, airframe which houses all the components has vital importance. This airframe can have two configurations as described in figure (3.1):

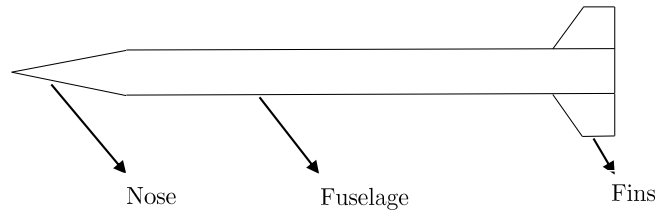
- Configuration I : Ogive-cylinder fuselage-fins
- Configuration II : Ogive-cylinder fuselage-wings-fins

Configuration II can again be of two types: one with 0 degree relative angle between fins and wings while other with some relative angle.

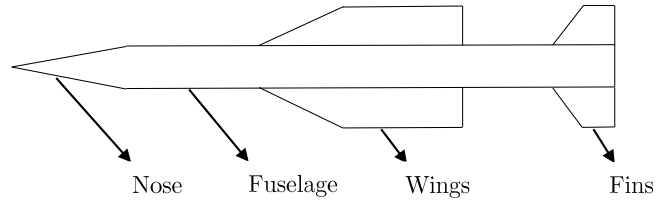
Again, tactical missiles can be classified on the basis of airframe structure as shown in figure (3.2):

- Cruciform
- Planform

Cruciform missiles are those that have the fin surfaces in case of both configurations and wing surfaces in case of configuration II at 90 degrees from each other. Planform missiles are those that have these surfaces at 180 degrees.



Configuration I : Ogive-cylinder fuselage-fins



Configuration II : Ogive-cylinder fuselage-wings-fins

Figure 3.1: Tactical Missile Configurations

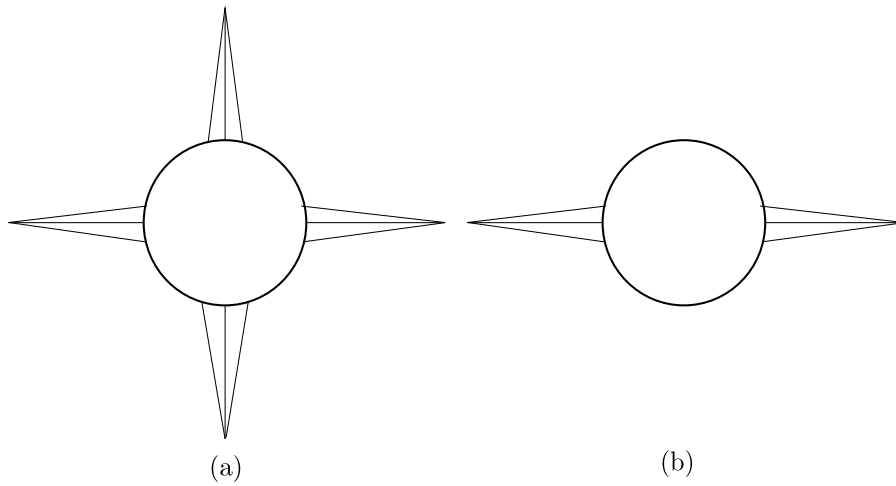


Figure 3.2: Types of Missile:
 (a) Cruciform Missile, (b) Planform Missile

The positioning of the missile can be defined by two quantities – angle of attack (α) and roll angle (φ). Centreline of cylindrical body of the missile coincides with X-axis as presented in the figure (3.3).

α – Angle made by free stream velocity field with positive X-axis measured in XY plane

φ – Angle made by wing and fin with the Y-axis measured in YZ plane

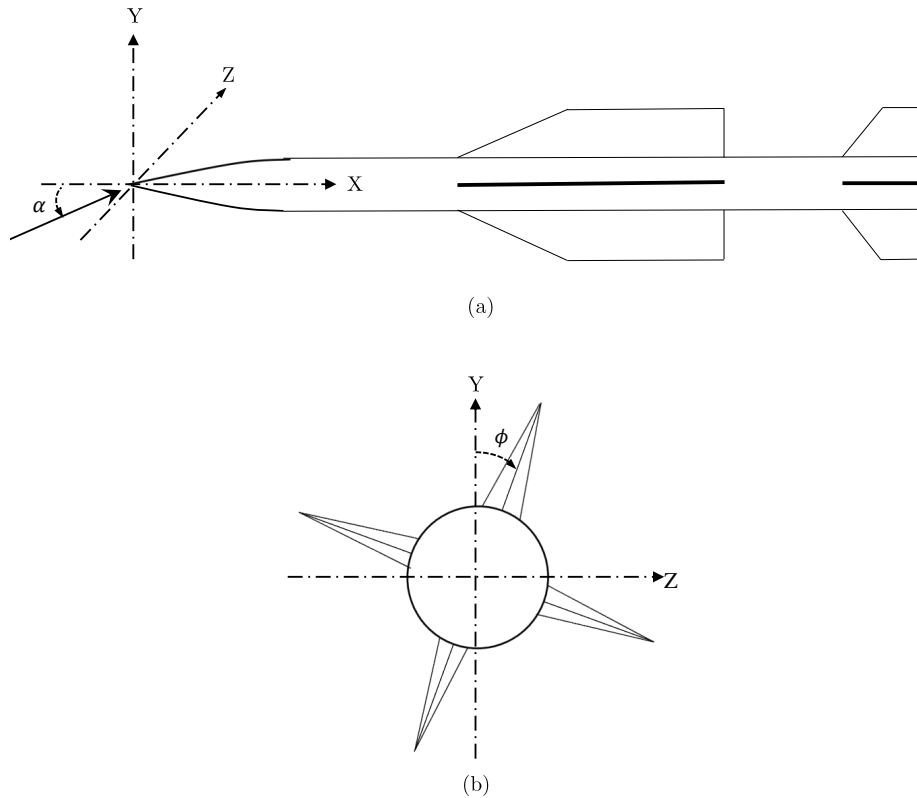


Figure 3.3: Angles Representation:
(a) Angle of Attack, (b) Roll Angle

3.2 Forces and Rolling Moment

While flying through the air, missile undergoes aerodynamic forces as well as moment. The rolling moment is an important factor for directionality.

3.2.1 Drag and Lift Forces

The forces experienced by missile are drag and lift forces which get generated due to skin-friction of air and due to pressure variation across the missile body. Drag is a force parallel to the flow of air while the lift is a force perpendicular to air flow. The drag force is the result of shearing action of air due to its viscous nature and also of form drag created by the pressure differences upon the surfaces. Lift is predominantly triggered by surface pressure differences.

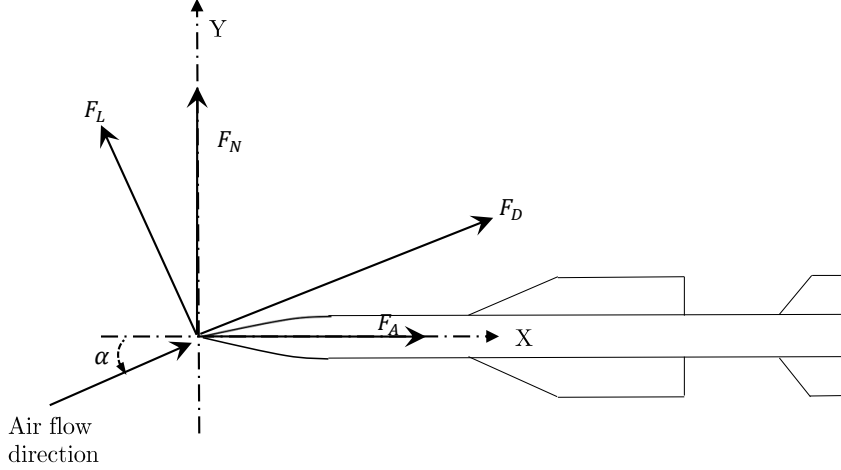


Figure 3.4: Forces Resolution

Figure (3.4) represents the resolution of drag force (F_D), lift force (F_L), axial force (F_A) and normal force (F_N). Relations between these forces can be derived as follows:

$$F_D = F_A \cos(\alpha) + F_N \sin(\alpha) \quad (3.1a)$$

$$F_L = F_N \cos(\alpha) - F_A \sin(\alpha) \quad (3.1b)$$

These axial and normal forces on the surface are calculated in the direction specified by the unit vector (\vec{a}) by summing up the dot product of specified direction vector with the pressure (\vec{F}_P) and viscous (\vec{F}_V) force vectors.

$$F_A = \vec{a} \cdot \vec{F}_P + \vec{a} \cdot \vec{F}_V \quad (3.2)$$

Pressure force and viscous force can be calculated from the following Equations eqs. (3.3a) and (3.3b):

$$\vec{F}_P = \int -P \vec{dA} \quad (3.3a)$$

$$\vec{F}_V = \int \tau_w \vec{dA} \quad (3.3b)$$

Wall shear stress can be estimated from shear velocity (u_τ) and density (ρ) as specified in equation (3.4a). Furthermore shear velocity can be determined by separate equations for different turbulence models and also it depends on the position of cell adjacent to wall surface. Equation (3.4b) provides relationship between non-dimensional velocity and non-dimensional wall distance while having wall adjacent cell centroid within laminar sublayer. If the centroid of wall adjacent cell exists within the

logarithmic region of boundary layer, law of the wall is applied which is given by equation (3.4c).

$$u_\tau = \sqrt{\frac{\tau_w}{\rho}} \quad (3.4a)$$

$$u^+ = y^+ \quad (3.4b)$$

$$u^+ = \frac{1}{\kappa} \ln(E \cdot y^+) \quad (3.4c)$$

$$u^+ = \frac{u}{u_\tau}; \quad y^+ = \frac{\rho u_\tau y}{\mu}; \quad \kappa = \text{Von Karman Constant}; \quad E = \text{Constant} \quad (3.4d)$$

Enhanced wall functions accompanied by the combined effect of the laminar as well as turbulent boundary layer can also be employed.

3.2.2 Rolling Moment

The rolling motion of missile is generated due to the vortices interaction with the wings and fins. At a small angle of attack, flow separation is not inevitable and hence the vortices. But noteworthy vortex shedding originates when the angle of attack increases. If the roll angle deviates from 0 (position '+') or 45 (position '×') degree, the interaction of vortices and the surfaces of fins and wings initiates the rolling moment as forces on the surfaces act unsymmetrically. It reaches critical at a roll angle of 22.5 degree.

Moment is the cross product of radial vector (\vec{r}_o) from considered axis which central axis of missile in the case of rolling moment and forces (\vec{F}_P and \vec{F}_V) acting on the walls of missile.

$$\vec{M} = \vec{r}_o \times \vec{F}_P + \vec{r}_o \times \vec{F}_V \quad (3.5)$$

3.3 Coefficients

The targeted values for the sensitivity analysis are coefficient of drag (C_D), coefficient of lift (C_L) and coefficient of rolling moment (C_m). The formulae for their calculation are expressed by equations 3.6a to 3.6c:

$$C_D = \frac{|F_D|}{\frac{1}{2} \rho A u^2} \quad (3.6a)$$

$$C_L = \frac{|F_L|}{\frac{1}{2} \rho A u^2} \quad (3.6b)$$

$$C_m = \frac{|\vec{M}|}{\frac{1}{2} \rho A u^2 L} \quad (3.6c)$$

Here A is cross-sectional area of fuselage and can be calculated by $\frac{\pi}{4} D^2$ where D is diameter of fuselage. The targeted output values are these dimensionless coefficients (C_m , C_D and C_L) and the sensitivity analysis is carried out for these coefficients.

3.4 Geometrical Elucidation

The geometry of the missile has been taken from Khelil et al. [16]. The present study deals with the cruciform missile with configuration II i.e. ogive-cylinder fuselage-wings-fins. Figure (3.5) illustrates the geometrical dimensions of missile overall body, wing, and fin. All the dimensions are stated in terms of D which is the diameter of missile fuselage and has been taken as 35 cm.

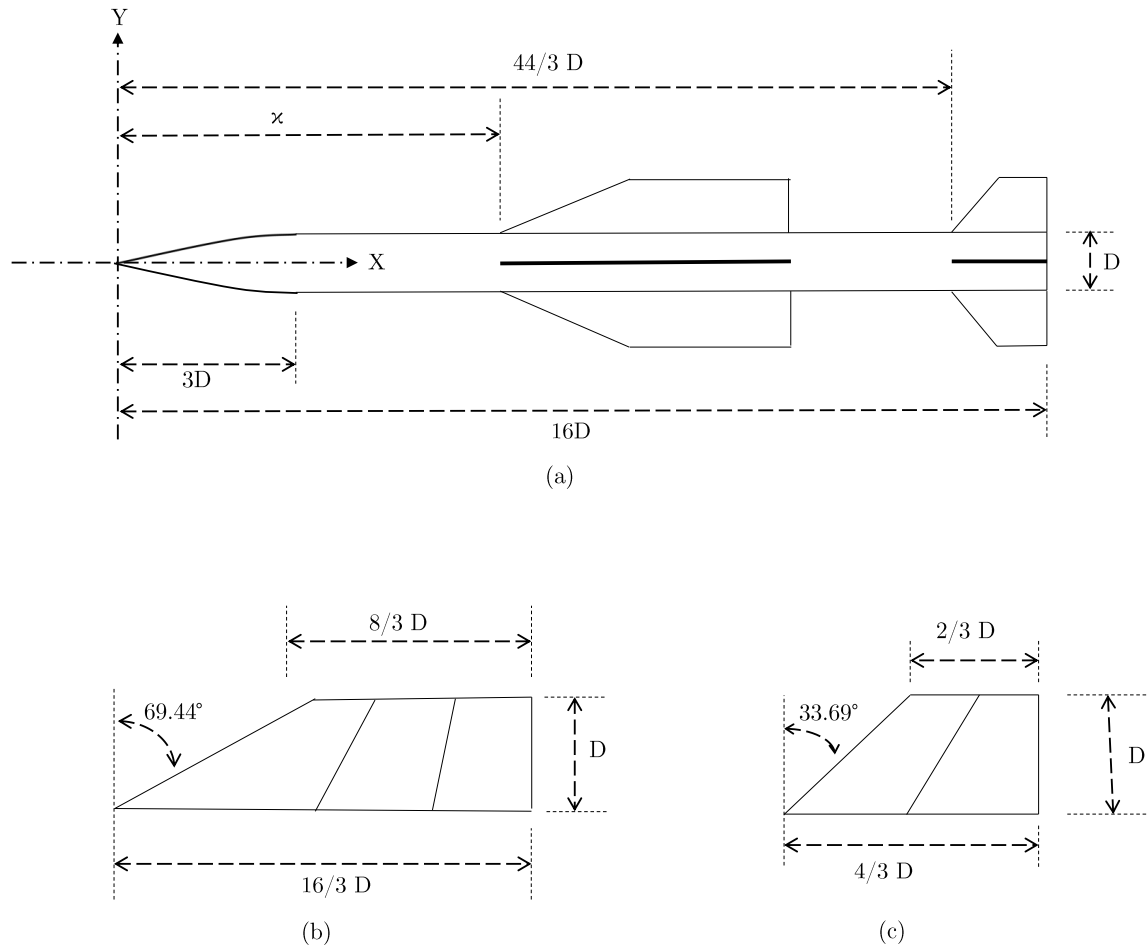


Figure 3.5: Geometrical Representation: (a) Missile Body Dimensions, (b) Wing Dimensions, and (c) Fin Dimensions

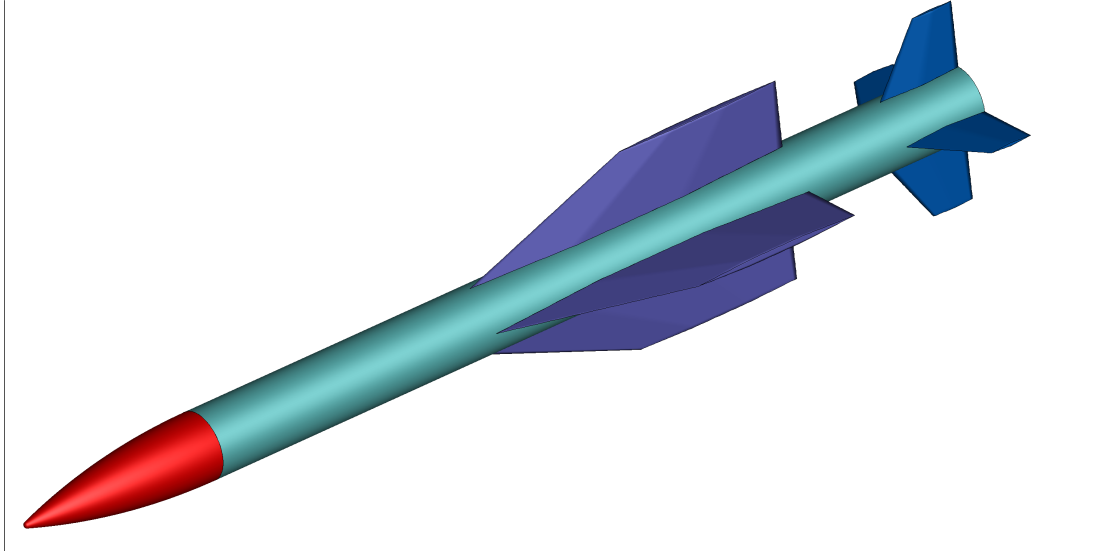


Figure 3.6: Missile Geometry

The wings in missile are located close to the center of gravity of missile and its deflection provides lift for manoeuvring flight. The wings and fins are of the clipped delta type. The cross section of wings is modified double wedge which consists the sharp leading and trailing edges. Fins are comprised of the double wedge with both sharp leading and trailing edges. Sharp edges help to maintain shock attachment, thereby reducing form drag and adverse pressure gradients.

Nose is of ogival shaped which is analogous to conical shape except that its planform shape is improved by an arc of the circle instead of a straight line. The advantage of the blunter nose is that it can withstand high thermal stresses which provide structural superiority over the conical nose.

3.5 Problem Definition

The flow of air over the missile is supersonic, turbulent. The diameter of fuselage cylinder (D) is taken as 35 cm. Boundary conditions for the problem are taken from Khelil et al. [16] and are mentioned in table (3.1):

Table 3.1: Boundary Conditions

Boundary Condition	Value
Mach number (M)	2
Angle of attack (α)	21.7 degree
Roll angle (ϕ)	22.5 degree
Stagnation pressure ($P_{T\infty}$)	1.8 bar
Stagnation temperature ($T_{T\infty}$)	300 K

The Reynolds number calculated on the basis of fuselage diameter can be given as

$$Re = \frac{\rho u D}{\mu} \quad (3.7a)$$

$$= 8.0 \times 10^6$$

$$\text{Reference velocity, } u = M \cdot \sqrt{\gamma R T_{T\infty}} \quad (3.7b)$$

Here, the specific gas constant of air (R) and adiabatic index (γ) are taken as 287.058 J/kgK and 1.4 respectively. Viscosity and density of air are taken as $1.7894e^{-05}$ Pa·s and 1.225 kg/m³ respectively.

Static pressure (P_∞) and static temperature (T_∞) required for farfield boundary condition are evaluated from isentropic flow relations (3.8a) and (3.8b).

$$P_\infty = P_\infty \left(1 + \frac{\gamma - 1}{2} M^2\right)^{-\gamma/(\gamma-1)} \quad (3.8a)$$

$$T_\infty = T_\infty \left(1 + \frac{\gamma - 1}{2} M^2\right)^{-1} \quad (3.8b)$$

From these relations, inlet static pressure (P) and static temperature (T_∞) come out to be 23004.81 Pa and 166.67 K respectively.

As this presented work mainly focuses on the sensitivity analysis in which the influence of different parameters is considered, the experimental results are not intended to achieve. Also, the results can not be compared with the experimental values since the distance of wing from the fore-body tip and the fore-body geometrical description is unspecified in the source of geometry.

3.6 Essentials

All the simulations are run using a well-tested computational fluid dynamics software ANSYS FLUENT 13.0.0.

Chapter 4

GCI And Identification Of Uncertainty Sources

In this chapter, brief discusses the methodology to encompass grid independence quantification, identification of uncertain input parameters and their range to study the sensitivity analysis.

4.1 Grid Independence Study

CFD employs discretization to transform PDEs of continuum formulation into a set of algebraic equations. Discretization error is governed by the meshing size used. It is subjected to the more adverse condition if the mesh is not fine enough. But at the same instance, the grid should not be too fine which ultimately intensifies the computational costs. Thus, it is imperative to investigate the effect of grid size on results.

4.1.1 Richardson Extrapolation

Richardson [33] proposed the Richardson Extrapolation (RE) and it is applicable to develop the formulae for Grid Convergence Index (GCI).

Suppose that the dependent output variable, ψ is a continuous and differential function of the representative grid size (h). Discrete solution for ψ can be expressed in a series of h as in Equation (4.1).

$$\psi_{Ext} = \psi_h + C_1 h + C_2 h^2 + C_3 h^3 + \dots \quad (4.1)$$

The exact value of the variable can be attained if the grid size tends to zero which is challenging to solve using available computational facilities. Error between the extrapolated value (ψ_{Ext}) and the approximate output value of variable (ψ_h) on the finite grid size avoiding the higher order terms can be given as:

$$\xi = \psi_{Ext} - \psi_h = C h^n + \mathcal{O}(h^{n+1}) \quad (4.2)$$

Here, n accounts for the apparent order of accuracy depends on the discretization schemes used for the simulations and C is a constant. Consider three different grids with grid sizes (h_1 , h_2 and

h_3) which are corresponding to fine, coarse and coarser grids respectively ($h_1 < h_2 < h_3$). The output values on these grids are ψ_1 , ψ_2 and ψ_3 respectively. Equations 4.3a to 4.3c represent the error formulae for the grids.

$$\xi_1 = \psi_{Ext} - \psi_1 = C h_1^n \quad (4.3a)$$

$$\xi_2 = \psi_{Ext} - \psi_2 = C h_2^n \quad (4.3b)$$

$$\xi_3 = \psi_{Ext} - \psi_3 = C h_3^n \quad (4.3c)$$

Subtracting equation (4.3a) from (4.3b) and (4.3b) from (4.3c) and rearranging the equations after taking log on both sides.

$$n = \frac{1}{\ln(r_{21})} \left| \ln \left| \frac{\psi_{32}}{\psi_{21}} \right| - \ln \left(\frac{r_{32}^n - s}{r_{21}^n - s} \right) \right| \quad (4.4)$$

$$\text{where, } r_{21} = \frac{h_2}{h_1}; r_{32} = \frac{h_3}{h_2} \quad (4.5a)$$

$$\xi_{21} = \xi_2 - \xi_1 = \psi_2 - \psi_1; \xi_{32} = \xi_3 - \xi_2 = \psi_3 - \psi_2 \quad (4.5b)$$

$$s = \text{sgn} \left(\frac{\xi_{32}}{\xi_{21}} \right) \quad (4.5c)$$

Equation (4.4) along with equations 4.5a to 4.5c gives the apparent order of scheme, n . Its value must be within the range of order of accuracy used in discretizing the flow field.

It is inconvenient to calculate the refinement factor (r) from the grid sizes (h), as it grid size may not be uniform for entire domain. Roache [34] has elucidated the refinement factor as stated by equation (4.6) for any dimensional (d) study.

$$r_{21} = \left(\frac{N_1}{N_2} \right)^{\frac{1}{d}}; r_{32} = \left(\frac{N_2}{N_3} \right)^{\frac{1}{d}} \quad (4.6)$$

Here, sgn is signum function. Implication of signum function is to extract the sign of the real number. It signifies when the convergence is of oscillatory type. Oscillatory convergence is the decrease of error with an alternating sign that is when ξ_{21} and ξ_{32} having alternating signs. It may take place due to the insufficient grid resolution in the required region of flow for a particular grid size.

$$\text{sgn} \left(\frac{\xi_{32}}{\xi_{21}} \right) = \begin{cases} -1 & \text{if } \left(\frac{\xi_{32}}{\xi_{21}} \right) < 0 \\ 0 & \text{if } \left(\frac{\xi_{32}}{\xi_{21}} \right) = 0 \\ 1 & \text{if } \left(\frac{\xi_{32}}{\xi_{21}} \right) > 0 \end{cases} \quad (4.7)$$

Uncertainty due to grid sizes can be reported using numerous methods. Extrapolated value for a variable can be obtained by implementing Richardson extrapolation and indicated in equation (4.8a). Approximate relative error (ξ_a^{21}) and extrapolated relative error (ξ_{Ext}^{21}) can be estimated

using equations 4.8b and (4.8c) respectively.

$$\psi_{Ext}^{21} = \frac{r_{21}^n \cdot \psi_1 - \psi_2}{r_{21}^n - 1}; \quad \psi_{Ext}^{32} = \frac{r_{32}^n \cdot \psi_2 - \psi_3}{r_{32}^n - 1} \quad (4.8a)$$

$$\xi_a^{21} = \left| \frac{\psi_1 - \psi_2}{\psi_1} \right| \quad (4.8b)$$

$$\xi_{Ext}^{21} = \left| \frac{\psi_{Ext}^{21} - \psi_1}{\psi_{Ext}^{21}} \right| \quad (4.8c)$$

4.1.2 Grid Convergence Index

GCI proposed by Roache [35] is an another measure to express the error due to grid refinement. Ching-Fang et al. [36] have implemented GCI for airfoil performance calculations and shown GCI to be a good measure with an advantage of non-integer grid refinement. GCI for fine grid solution can be determined by equation (4.9)

$$GCI_{fine}^{21} = \frac{F_S \cdot \xi_a^{21}}{r_{21}^n - 1} \quad (4.9)$$

F_S is the factor of safety and it should be greater than one. GCI was originally proposed by Roache [35] with $F_S = 3$ which is advantageous since it relates any grid convergence study (with any n and r) to the one with a grid doubling ($r = 2$) and a second order method ($n = 2$). But it can be safely taken as 1.25 as given in [12].

Sometimes it is impractical to use fine grid due to limited resources or time. Therefore, the use of a coarse grid solution is cheap to run by having just one fine grid solution for reference. For such purpose, coarse grid GCI can be defined by,

$$GCI_{fine}^{21} = \frac{F_S \cdot \xi_a^{21} \cdot r_{21}^n}{r_{21}^n - 1} \quad (4.10)$$

4.1.3 Steps to Calculate GCI

The current work follows the steps mentioned below:

- a. Generate the meshes with fine (N_1), coarse (N_2) and coarser (N_3) cell nodes such that (r_{21}) and (r_{32}) should be close to 1.3 i.e. 30% grid size difference between consecutive meshes. Three meshes should have same the distribution of cell nodes.
- b. Perform the simulations for three meshes and report the output variable which are the coefficient of rolling moment, the coefficient of drag and coefficient of lift for the current work of missile aerodynamics.
- c. Calculate the apparent order of scheme, n .
- d. Report the extrapolated values using equations (4.8a).

- e. Report the uncertainty due to the grid using equations (4.8b), (4.8c) and (4.9) or (4.10). Equation (4.9) can be used if the fine mesh is affordable to use for the further work or else equation (4.10) can be used.

4.2 Geometrical Sensitivity

Geometrical sensitivity parameter here is the distance of wings from the fore-body tip (κ). The distance κ is not given in literature [16]. It is taken as $23D/3$ and is perturbed by $2D/3$.

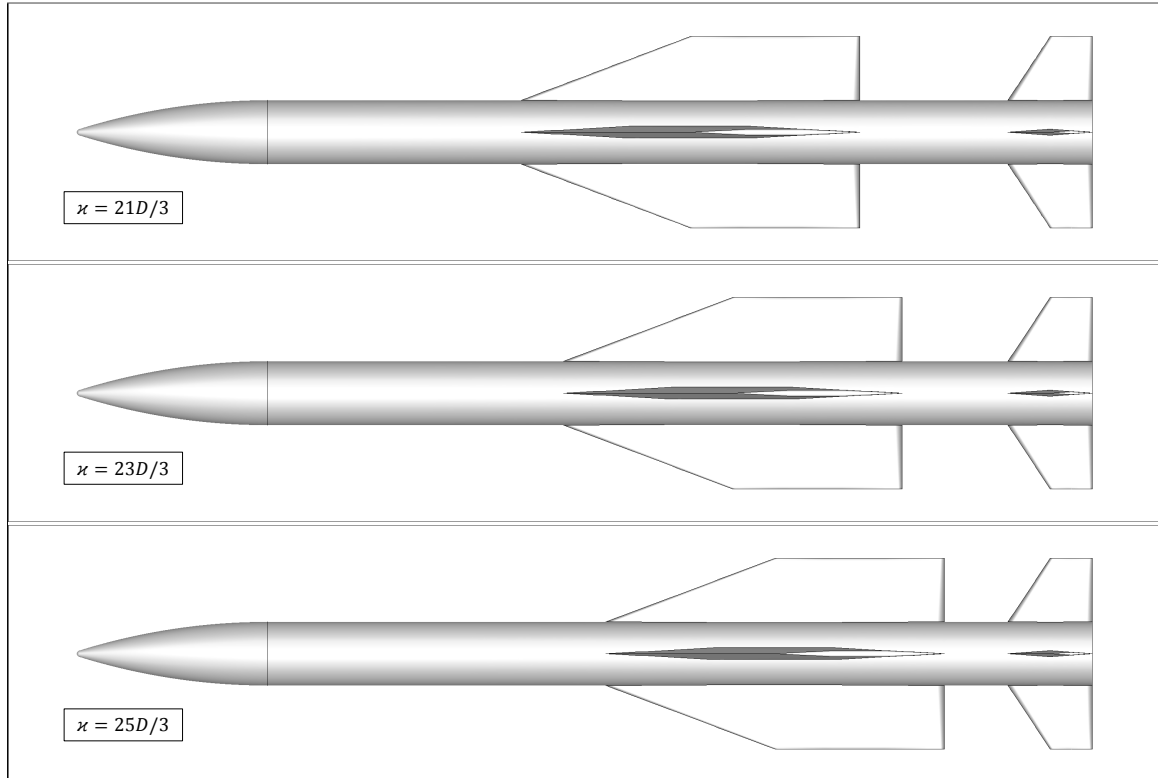


Figure 4.1: Geometrical Sensitivity

4.3 Turbulence Modelling

Air flow over the missile is supersonic and hence, the shock phenomenon should be considered while using turbulence model. Shock exhibits the adverse pressure gradient in the flow.

As Large Eddy Simulations (LES) and Direct Numerical Solution (DNS) necessitates high computational effort, it is inconvenient to use for the industrial problems. Nevertheless, Reynolds-Averaged Navier-Stoke (RANS) approach provides a solution with far less computational effort. But at the same time, there is a compromise with the accuracy of results. This section deals with the introduction to the advantages of certain turbulence models as well as the effect of another parameter such as turbulent intensity (TI).

4.3.1 RANS and Boussinesq Approximation

In turbulent flow, field variable such as velocity, pressure, and temperature become a random function of space and time. Therefore, they can be separated into two viz., mean (time-averaged) and fluctuating components.

$$u = \bar{u}_i + u'_i ; P = \bar{P} + P' ; T = \bar{T} + T' \quad (4.11)$$

By taking the time average of continuity equation, Navier-Stoke equation, and energy equation, a set of three equations is arrived.

For the compressible flow, these field variables can be Favre-averaged which is nothing but a density-weighted averaging.

$$u = \tilde{u}_i + u''_i ; P = \tilde{P} + P'' ; T = \tilde{T} + T'' \quad (4.12a)$$

$$\text{where, } \tilde{u}_i = \frac{\overline{\rho u_i}}{\bar{\rho}} ; \tilde{P} = \frac{\overline{\rho P}}{\bar{\rho}} ; \tilde{T} = \frac{\overline{\rho T}}{\bar{\rho}} \quad (4.12b)$$

By taking the Favre-average of continuity equation, Navier-Stoke equation, and energy equation, a set of three equations arrives.

$$\frac{\partial \bar{\rho}}{\partial t} + \frac{\partial(\bar{\rho} \tilde{u}_i)}{\partial x_i} = 0 \quad (4.13a)$$

$$\frac{\partial(\bar{\rho} \tilde{u}_i)}{\partial t} + \frac{\partial(\tilde{u}_j \bar{\rho} \tilde{u}_i)}{\partial x_j} = -\frac{\partial \tilde{P}}{\partial x_i} + \frac{\partial \overline{\sigma_{ij}}}{\partial x_j} + \frac{\partial \tau_{ij}}{\partial x_j} \quad (4.13b)$$

$$\frac{\partial(\bar{\rho} \tilde{E})}{\partial t} + \frac{\partial \left[\tilde{u}_j \bar{\rho} (\tilde{E} + \tilde{P}/\bar{\rho}) \right]}{\partial x_j} = \frac{\partial \left(\overline{\sigma_{ij} \tilde{u}_i} + \overline{\sigma_{ij} u''_i} \right)}{\partial x_j} - \frac{\partial}{\partial x_j} \left(-\frac{c_p \tilde{\mu}}{Pr} \frac{\partial \tilde{T}}{\partial x_j} + \overline{c_p \rho u''_j T''} - \tilde{u}_i \tau_{ij} + \frac{1}{2} \overline{\rho u''_i u''_i u''_j} \right) \quad (4.13c)$$

Viscous stress tensor ($\overline{\sigma_{ij}}$) is given by,

$$\overline{\sigma_{ij}} = 2\tilde{\mu} \left[\tilde{S}_{ij} - \frac{1}{3} \delta_{ij} \frac{\partial \tilde{u}_k}{\partial x_k} \right] \quad (4.13d)$$

and the Reynolds stress term (τ_{ij}) based on Boussinesq approximation can be expressed as,

$$\tau_{ij} = 2\tilde{\mu}_t \left[\tilde{S}_{ij} - \frac{1}{3} \delta_{ij} \frac{\partial \tilde{u}_k}{\partial x_k} \right] - \frac{2}{3} \bar{\rho} k \delta_{ij} \quad (4.13e)$$

where δ_{ij} is Kronecker delta and is equal to one if $i = j$ and zero otherwise. Strain rate tensor (\tilde{S}_{ij}) is,

$$\tilde{S}_{ij} = \frac{1}{2} \left(\frac{\partial \tilde{u}_i}{\partial x_j} + \frac{\partial \tilde{u}_j}{\partial x_i} \right) \quad (4.13f)$$

The Reynolds stress term comprises of the turbulent viscosity $\tilde{\mu}_t$. The turbulent viscosity is

then modelled with different models with their own advantages and disadvantages. Considering the compressible flow with adverse pressure gradients in shock region, the Spalart Allmaras model, and $k - \omega$ model are suitable.

4.3.2 Spalart Allmaras Model

Spalart Allmaras model [17] is one-equation model and holds good applicability in wall-bounded flows. It includes the wall function in the case of insufficient mesh resolution. Modification [37] in the turbulent production term reflects the effect of both vorticity and strain tensors. Spalart Allmaras model is expressed by equations (4.14a) to (4.14k).

$$\frac{\partial(\rho\tilde{\nu})}{\partial t} + \frac{\partial(u_j\rho\tilde{\nu})}{\partial x_j} = C_{b1}\tilde{S}\rho\tilde{\nu} - C_{w1}f_w\rho\left(\frac{\tilde{\nu}}{d}\right)^2 + \frac{1}{\sigma_{\tilde{\nu}}}\left[\frac{\partial}{\partial x_j}\left((\mu + \rho\tilde{\nu})\frac{\partial\tilde{\nu}}{\partial x_j}\right) + C_{b2}\rho\left(\frac{\partial\tilde{\nu}}{\partial x_j}\right)^2\right] \quad (4.14a)$$

The turbulent viscosity (μ_t) is calculated from:

$$\mu_t = \rho\tilde{\nu}f_{v1} \quad (4.14b)$$

The supplementary equations are:

$$f_{v1} = \frac{\chi^3}{\chi^3 + C_{v1}^3}; \quad \chi = \frac{\tilde{\nu}}{\nu} \quad (4.14c)$$

$$\tilde{S} = S + \frac{\tilde{\nu}}{k^2d^2}f_{v2} \quad (4.14d)$$

$$S = |\Omega_{ij}| + 2 \cdot \min(0, |S_{ij}| - |\Omega_{ij}|); \quad f_{v2} = 1 - \frac{\chi}{1 + \chi f_{v1}} \quad (4.14e)$$

$$S_{ij} = \frac{1}{2}\left(\frac{\partial u_i}{\partial x_j} + \frac{\partial u_j}{\partial x_i}\right); \quad \Omega_{ij} = \frac{1}{2}\left(\frac{\partial u_i}{\partial x_j} - \frac{\partial u_j}{\partial x_i}\right) \quad (4.14f)$$

$$f_w = g\left(\frac{1 + C_{w3}^6}{g^6 + C_{w3}^6}\right)^{1/6} \quad (4.14g)$$

$$g = r + C_{w2}(r^6 - r); \quad r = \frac{\tilde{\nu}}{\tilde{S}k^2d^2} \quad (4.14h)$$

$$C_{w1} = \frac{C_{b1}}{k^2} + \frac{1 + C_{b2}}{\sigma_{\tilde{\nu}}} \quad (4.14i)$$

and constants are:

$$C_{b1} = 0.1355; \quad C_{b2} = 0.622; \quad \sigma_{\tilde{\nu}} = \frac{2}{3}; \quad C_{v1} = 7.1 \quad (4.14j)$$

$$C_{w2} = 0.3; \quad C_{w3} = 2.0; \quad k = 0.4187 \quad (4.14k)$$

4.3.3 Standard $k - \omega$ Model

Standard $k - \omega$ model [20] [38] gives close agreement of flow prediction with the experimental results for the cases of free shear flows and wall-bounded flows. It comprises of two transport equations: (a) for k – the turbulent kinetic energy; and (b) for ϵ – the specific dissipation rate.

$$\frac{\partial(\rho k)}{\partial t} + \frac{\partial(u_j \rho k)}{\partial x_j} = \tau_{ij} \frac{\partial u_i}{\partial x_j} - \beta^* f_{\beta^*} \rho \omega k + \frac{\partial}{\partial x_j} \left[\left(\mu + \sigma_k \frac{\rho k}{\omega} \right) \frac{\partial k}{\partial x_j} \right] \quad (4.15a)$$

$$\frac{\partial(\rho \omega)}{\partial t} + \frac{\partial(u_j \rho \omega)}{\partial x_j} = \frac{\gamma \omega}{k} \tau_{ij} \frac{\partial u_i}{\partial x_j} - \beta f_b \rho \omega^2 + \frac{\partial}{\partial x_j} \left[\left(\mu + \sigma_\omega \frac{\rho k}{\omega} \right) \frac{\partial \omega}{\partial x_j} \right] \quad (4.15b)$$

The turbulent viscosity (μ_t) is calculated from:

$$\mu_t = \frac{\rho k}{\omega} \quad (4.15c)$$

The supplementary equations are:

$$f_{\beta^*} = \begin{cases} 1 & \text{if } \chi_k \leq 0 \\ \frac{1+680\chi_k^2}{1+400\chi_k^2} & \text{if } \chi_k > 0 \end{cases} \quad (4.15d)$$

$$\chi_k = \frac{1}{\omega^3} \frac{\partial k}{\partial x_j} \frac{\partial \omega}{\partial x_j} \quad (4.15e)$$

$$\beta^* = 0.09 \left(\frac{4/15 + (Re_t/Re_\beta)^4}{1 + (Re_t/Re_\beta)^4} \right); \quad Re_t = \frac{\rho k}{\mu \omega} \quad (4.15f)$$

$$f_b = \frac{1 + 70\chi_\omega}{1 + 80\chi_\omega}; \quad \chi_\omega = \left| \frac{\Omega_{ij} \Omega_{jk} S_{ki}}{(0.09 \omega)^3} \right| \quad (4.15g)$$

The constants are as follows:

$$\sigma_k = 0.5; \quad \sigma_\omega = 0.5; \quad Re_\beta = 8.0 \quad (4.15h)$$

4.3.4 SST $k - \omega$ Model

Shear Stress Transport $k - \omega$ model [39] is the blending of standard $k - \omega$ and $k - \epsilon$ model. Standard $k - \omega$ is activated in the near wall region while $k - \epsilon$ is activated the region away from wall by invalidating the $k - \omega$ model. This is done to take the advantages of both models and makes it more accurate in the near-wall region as well as in far-field region. SST $k - \omega$ model consists a crossed diffusion derivative term in the transport equation of ω . The formulations for the model are expressed by equations (4.16a) to (4.16i):

$$\frac{\partial(\rho k)}{\partial t} + \frac{\partial(u_j \rho k)}{\partial x_j} = \tilde{G} - \beta^* \rho \omega k + \frac{\partial}{\partial x_j} \left[(\mu + \sigma_k \mu_t) \frac{\partial k}{\partial x_j} \right] \quad (4.16a)$$

$$\frac{\partial(\rho \omega)}{\partial t} + \frac{\partial(u_j \rho \omega)}{\partial x_j} = \frac{\alpha}{\nu_t} \tilde{G} - \beta \rho \omega^2 + \frac{\partial}{\partial x_j} \left[(\mu + \sigma_\omega \mu_t) \frac{\partial \omega}{\partial x_j} \right] + 2(1 - F_1) \frac{\rho \sigma_{\omega 2}}{\omega} \frac{\partial k}{\partial x_j} \frac{\partial \omega}{\partial x_j} \quad (4.16b)$$

The turbulent viscosity (μ_t) is calculated from:

$$\mu_t = \frac{\rho a_1 k}{\max(a_1 \omega, S_{ij} F_1)} \quad (4.16c)$$

The supplementary equations are:

$$\tilde{G} = \min \left(\tau_{ij} \frac{\partial u_i}{\partial x_j}, 10 \rho \beta^* k \omega \right) \quad (4.16d)$$

$$\sigma_k = F_1 / \sigma_{k1} + (1 - F_1) / \sigma_{k2} ; \sigma_\omega = F_1 / \sigma_{\omega 1} + (1 - F_1) / \sigma_{\omega 2} \quad (4.16e)$$

$$F_1 = \tanh \left(\Phi_1^4 \right) ; \Phi_1 = \min \left[\max \left(\frac{\sqrt{k}}{0.09 \omega y}, \frac{500 \mu}{\rho y^2 \omega} \right), \frac{4 \rho k}{\sigma_{\omega 2} D_\omega^+ y^2} \right] \quad (4.16f)$$

$$D_\omega^+ = \max \left(2 \rho \frac{1}{\omega \sigma_{\omega 2}} \frac{\partial k}{\partial x_j} \frac{\partial \omega}{\partial x_j}, 10^{-10} \right) \quad (4.16g)$$

$$F_2 = \tanh \left(\Phi_2^2 \right) ; \Phi_2 = \max \left(2 \frac{\sqrt{k}}{0.09 \omega y}, \frac{500 \mu}{\rho y^2 \omega} \right) \quad (4.16h)$$

and constants are:

$$\sigma_{k1} = 1.176 ; \sigma_{\omega 1} = 2.0 ; \sigma_{k2} = 1.0 ; \sigma_{\omega 2} = 1.168 ; a_1 = 0.31 \quad (4.16i)$$

4.3.5 Turbulent Intensity

Turbulent intensity (I) is the ratio of the root mean square of turbulent velocity fluctuation (u') and the mean velocity (u). Turbulent intensity is required to found out the boundary conditions for the turbulent variables like $\tilde{\nu}$, k , and ω .

$$I = \frac{u'}{u} \quad (4.17a)$$

where,

$$u' = \sqrt{\frac{1}{3} (u_i'^2 + u_j'^2 + u_k'^2)} ; u = \sqrt{\tilde{u}_i^2 + \tilde{u}_j^2 + \tilde{u}_k^2} \quad (4.17b)$$

For the case of external flow, I can be in the range of 0.5% to 1.5% and the sensitivity of I has been studied by Shao-wu LI et al. [24].

4.4 Viscosity Model

The molecular viscosity of the fluid is the temperature dependent quantity and here the viscosity of air is modelled using Sutherland's law, kinetic theory, and power-law.

4.4.1 Sutherland's Law

Sutherland's three coefficient law [27] provides the relationship between the molecular viscosity (μ) and absolute temperature (T_T) as follows:

$$\mu = \mu_{ref} \left(\frac{T_T}{T_{Tref}} \right)^{3/2} \left(\frac{T_{Tref} + S}{T_T + S} \right) \quad (4.18)$$

where for air,

$$\begin{aligned} \mu_{ref} &= \text{reference viscosity} = 1.716 \times 10^{-5} \text{ kg/m}\cdot\text{s} \\ T_{Tref} &= \text{reference stagnation temperature} = 273.11 \text{ K} \\ S &= \text{Sutherland's constant} = 110.56 \text{ K} \end{aligned}$$

Sutherland's law computes viscosity moderately for the wide range of temperature. It is valid only for ideal gas law.

4.4.2 Viscosity Modelling Using Kinetic Theory

Viscosity can be defined by the kinetic theory [40].

$$\mu = 2.67 \times 10^{-6} \cdot \frac{\sqrt{M_w T_T}}{\sigma^2 \omega T^*} \quad (4.19)$$

where,

$$\begin{aligned} T^* &= \frac{kT_T}{\epsilon} = \text{dimensionless reduced temperature} \\ M_w &= \text{molecular weight (g/mol)} \\ \sigma &= \text{the collision diameter (Angstroms)} \\ \omega &= \text{the collision integral} \end{aligned}$$

4.4.3 Power-Law Viscosity Model

Power-law viscosity formula with three coefficients is expressed as:

$$\mu = \mu_{ref} \left(\frac{T_T}{T_{Tref}} \right)^n \quad (4.20)$$

where for air,

$$\begin{aligned} \mu_{ref} &= \text{reference viscosity} = 1.716 \times 10^{-5} \text{ kg/m}\cdot\text{s} \\ T_{Tref} &= \text{reference stagnation temperature} = 273.11 \text{ K} \\ n &= 2/3 \end{aligned}$$

4.5 Thermal Conductivity Model

The thermal conductivity of air is 0.0242 W/m·K and can also be defined by the function of temperature. The models used here are kinetic theory and polynomial.

4.5.1 Thermal Conductivity Modelling Using Kinetic Theory

The thermal conductivity defined using kinetic theory is given as:

$$k = \frac{15R}{4M_w} \mu \left(\frac{4 \cdot c_p \cdot M_w}{15R} + \frac{1}{3} \right) \quad (4.21)$$

where,

R = universal gas constant

c_p = specific heat capacity at constant pressure

4.5.2 Thermal Conductivity Using Polynomial Of Temperature

Another approximation for the thermal conductivity calculation is given by the polynomial function of temperature:

$$k = A_1 + A_2 \cdot T_T + A_3 \cdot T_T^2 + \dots + A_8 \cdot T_T^7 \quad (4.22)$$

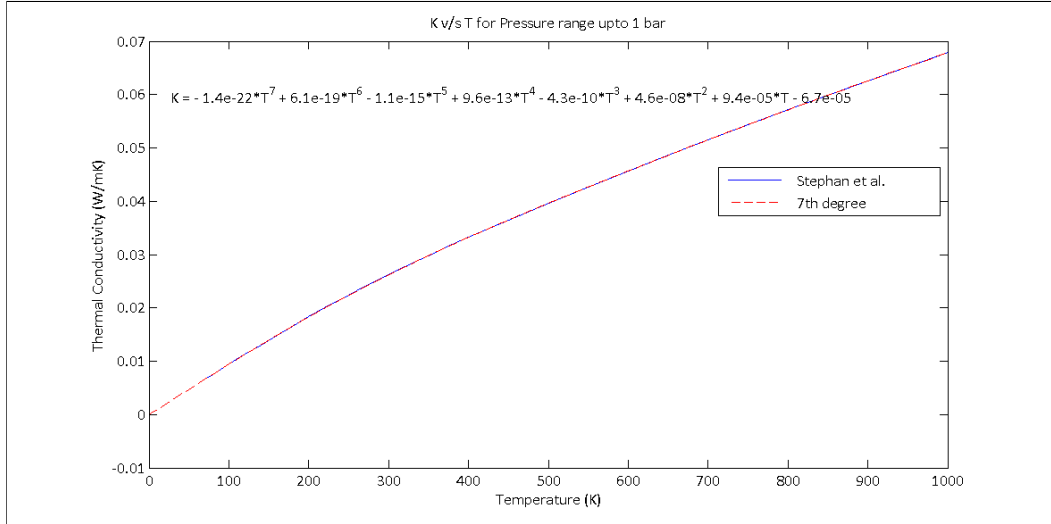


Figure 4.2: Thermal Conductivity as the Function of Temperature

The temperature polynomial used in the study is up to 7th degree and the coefficients taken from Stephan et al. [28] are as follows:

$$A_1 = -6.7 \times 10^{-5}; A_2 = 9.4 \times 10^{-5}; A_3 = 4.6 \times 10^{-8}; A_4 = -4.3 \times 10^{-10}; \\ A_5 = 9.6 \times 10^{-13}; A_6 = -1.1 \times 10^{-15}; A_7 = 6.1 \times 10^{-19}; A_8 = -1.4 \times 10^{-22}$$

4.6 Specific Heat

The specific heat of air at constant pressure is 1006.43 J/kg·K. Kinetic theory and piecewise polynomial function of temperature are used to define the specific heat.

4.6.1 Specific Heat Using Kinetic Theory

Kinetic theory formulation for the specific heat is:

$$c_p = \frac{R}{2M_w}(f + 2) \quad (4.23)$$

Here, f is the number of active degrees of freedom and is equal to 5 for air.

4.6.2 Piecewise Polynomial

Specific heat can also be defined as the function of temperature. The piecewise polynomial is used to derive the formula for the specific heat of air and is given by (??).

$$c_p = \begin{cases} A_1 + A_2 \cdot T_T + A_3 \cdot T_T^2 + \dots + A_8 \cdot T_T^7 & \text{if } 100K < T_T < 1000K \\ B_1 + B_2 \cdot T_T + B_3 \cdot T_T^2 + \dots + B_8 \cdot T_T^7 & \text{if } 1000K < T_T < 3000K \end{cases} \quad (4.24)$$

The coefficients are,

$$\begin{aligned} A_1 &= 1.16 \times 10^3; & A_2 &= -2.37 \times 10^1; & A_3 &= 1.49 \times 10^{-2}; & A_4 &= -5.04 \times 10^{-5}; \\ A_5 &= 9.93 \times 10^{-8}; & A_6 &= -1.11 \times 10^{-10}; & A_7 &= 6.54 \times 10^{14}; & A_8 &= -1.57 \times 10^{-17}; \\ B_1 &= -7.07 \times 10^3; & B_2 &= 3.37 \times 10^1; & B_3 &= -5.81 \times 10^{-2}; & B_4 &= 5.42 \times 10^{-5}; \\ B_5 &= -2.94 \times 10^{-8}; & B_6 &= 9.24 \times 10^{-12}; & B_7 &= -1.57 \times 10^{-15}; & B_8 &= 1.11 \times 10^{-19} \end{aligned}$$

4.7 Static Temperature Sensitivity

The static temperature estimated from stagnation pressure and stagnation temperature can also lead to uncertainty as the measurement techniques for these quantities may have an error. Rhode et al. [11] explained that the particular wind tunnel can have $\pm 0.1\%$ error in the measurement of stagnation pressure for the range of 0 – 137 bar and that for stagnation temperature is ± 2.2 K in the range of 70 K to 1500 K. Here static pressure is considered to be constant.

Uncertainty in the free stream static temperature (w_T) is evaluated by equation (4.25a).

$$w_T = \left[\left(\frac{\partial T}{\partial T_T} w_{T_T} \right)^2 + \left(\frac{\partial T}{\partial P_T} w_{P_T} \right)^2 \right]^{1/2} \quad (4.25a)$$

given that the static temperature is expressed by,

$$T = T_T \left(\frac{P_T}{P} \right)^{-(\gamma-1)/\gamma} \quad (4.25b)$$

where the uncertainty in stagnation pressure and stagnation temperature are,

$$w_{T_T} = 2.2 \text{ K} ; w_{P_T} = 1.8 \times 10^2 \text{ Pa} \quad (4.25c)$$

and free stream boundary conditions are,

$$P_T = 1.8 \text{ bar} ; T_T = 300 \text{ K} ; P = 23004.81 \text{ Pa} \quad (4.25d)$$

The derivatives are calculated as,

$$\frac{\partial T}{\partial T_T} = \left(\frac{P_T}{P} \right)^{-(\gamma-1)/\gamma} = 1.8 \quad (4.25e)$$

$$\frac{\partial T}{\partial P_T} = T_T \left(\frac{1-\gamma}{\gamma} \right) \left(\frac{P_T}{P} \right)^{(1-2\gamma)/\gamma} \frac{1}{P} = 2.6455 \times 10^{-4} \quad (4.25f)$$

The uncertainty in static temperature (w_T) is therefore equal to ± 3.96 K over $T = 166.67$ K.

4.8 Convective Flux Type

The inviscid fluxes in Navier-Stokes equation can be evaluated on each face of cells by using two approaches: (a) Roe Flux Difference Splitting scheme (Roe-FDS) [29], and (b) Advection Upstream Splitting Method (AUSM) [30]. AUSM+ is designed to calculate the inviscid fluxes accurately on the faces in the case of grid aligned to the geometry. But it is still under development if it is not aligned.

4.9 Order of Discretization Scheme

The first order upwind, second order upwind and third order MUSCL schemes are the alternatives for discretization of all the flow variables which are pressure, u -velocity, v -velocity, w -velocity, and temperature and the turbulent viscosity.

4.10 GSA Parameters

The Global Sensitivity Analysis is the process of perturbation of each input uncertainty parameter individually from its nominal value and examining its effect on output result. It is called as global since the output parameters considered which are coefficient of rolling moment (C_m), coefficient of drag (C_D) and coefficient of lift (C_L) are globally defined quantities.

The nominal case is derived from the best possible settings for the problem and from the nominal values. The table (4.1) summarizes the nominal case values of input variables with their perturbations from the above discussed theory. Out of nine parameters, the first seven are of type modelling uncertainty while last two are of type numerical uncertainty.

Table 4.1: GSA Parameters

No.	Uncertainty Sources	Perturbation #1	Nominal Case Value	Perturbation #2
1.	Geometrical Parameter (\varkappa)	21D/3	23D/3	25D/3
2.	Turbulence Model	Standard $k - \omega$	Spalart Allmaras	SST $k - \omega$
3.	Viscosity Model	Kinetic Theory	Sutherland	Power Law
4.	Thermal Conductivity	Kinetic Theory	Constant (0.0242 W/m·K)	Polynomial
5.	Specific Heat	Kinetic Theory	Constant (1006.43 J/kg·K)	Piecewise Polynomial
6.	Static Temperature	166.67 – 3.96 K	166.67 K	166.67 + 3.69 K
7.	Turbulence Intensity	0.5%	1%	1.5%
8.	Inviscid Flux Type	Roe-FDS	AUSM	–
9.	Discretization Scheme Order	1 st Order	2 nd Order	3 rd Order

Chapter 5

Nominal Case

This chapter explains the nominal case setup with the meshing and its results. The qualitative comparison of the nominal case results also made with Khelil et al. [16].

5.1 Mesh Generation

Missile body is enclosed with the computational domain of hemispherical inlet and cylindrical farfield as shown in figure (5.1). The radius of hemisphere is equal to $80D$ which is about 28 m. The tip of nose is situated at the coordinate $(0, 0, 0)$.

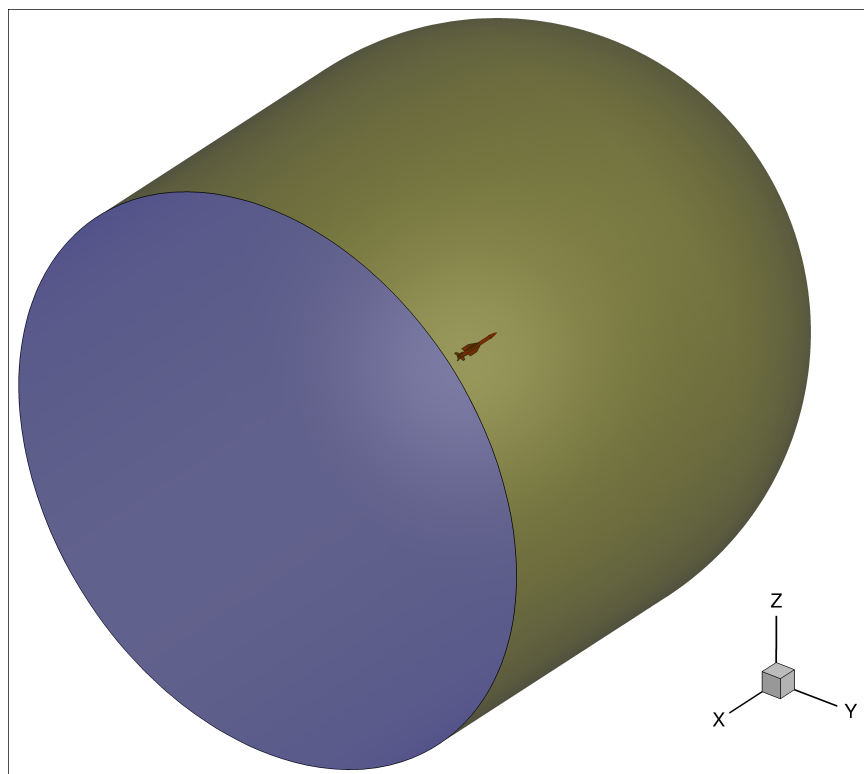


Figure 5.1: Missile with Computational Domain

The effect of farfield boundary condition is diminished due to the domain with such a quiet large hemispherical diameter.

The streamlined structured mesh is created for the domain. The radial edge from the missile surface is divided into 96 nodes with first node adjacent to fuselage wall is $4e^{-05}$ m from the wall and 1.3 as the advancement outward ratio up to tip of the wing and fins. The advancement is exponent after the wings and fins tip. The nose edge and fuselage edge is divided into 38 and 266 intervals in the lengthwise distance. The circumferential edge of fuselage cylinder is having 160 nodes is divided such a way that it is dense near surfaces of the wings and fins. The domain after the missile is having the edge divided into 66 intervals. y^+ value corresponding to $4e^{-05}$ m cell distance from is equal to about 8. The total number of nodes of the nominal case mesh is 5,316,960.

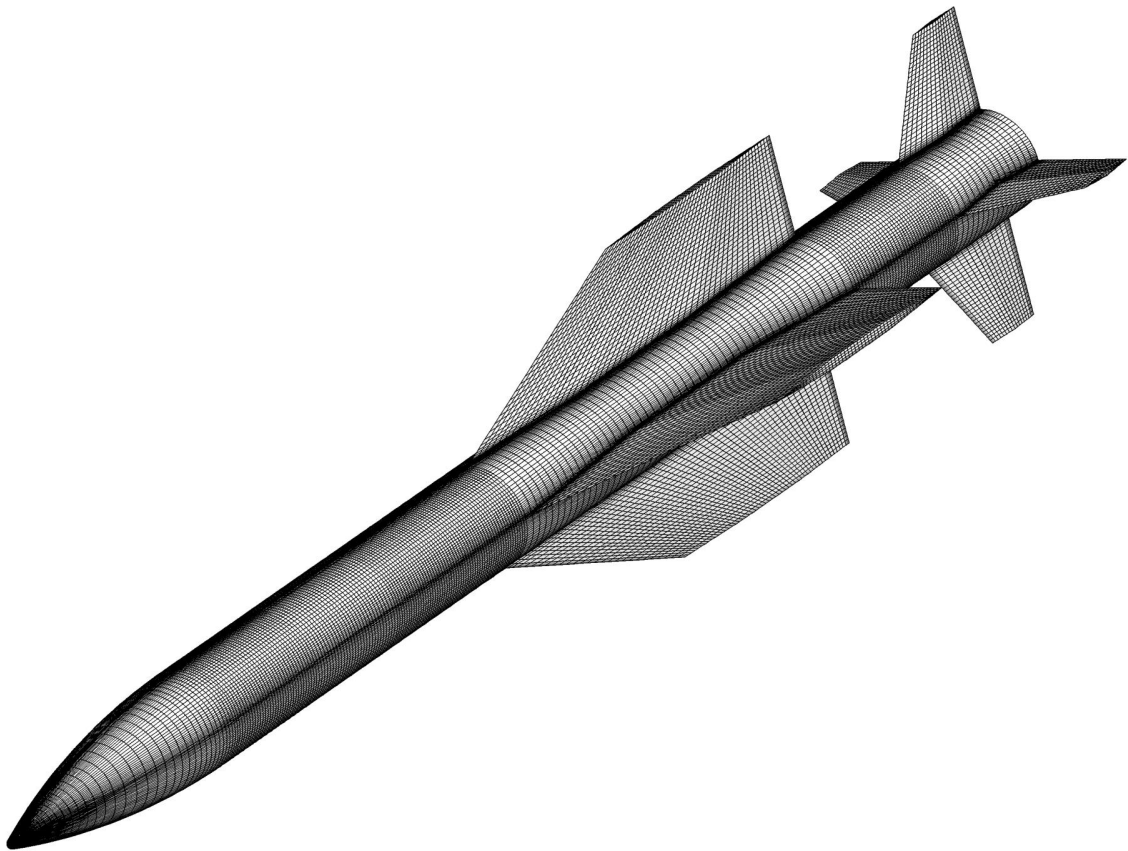


Figure 5.2: Meshing of Missile Body

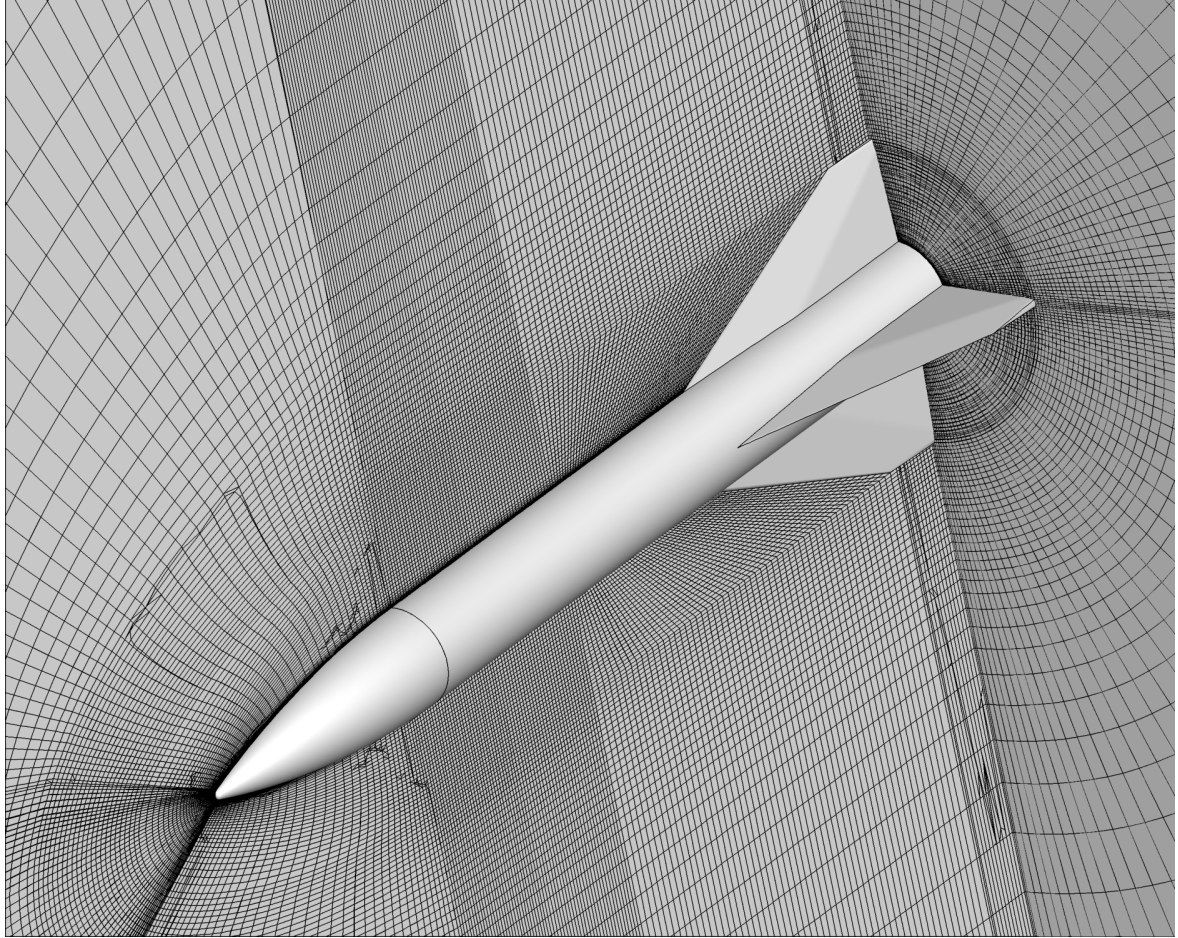


Figure 5.3: Meshing of Computational Domain

5.2 Solver Settings

The flow over missile is supersonic and as a consequence of this, the double precision density based solver is used as pressure based solver is suitable for the flow regime with mach number equal to around 0.9. The transient implicit formulation is used. The flow is simulated initially by considering it as inviscid and then switched to turbulent.

The parameters for nominal case are mentioned in the table (4.1). Low Reynold damping Spalart Allmaras turbulence model with strain/vorticity based production is used. The density of air is calculated by ideal gas law since the farfield only works with the ideal gas law. The inlet boundary condition is pressure farfield accompanied by pressure outlet for pressure. The angle of attack ($\alpha = 22.7$ degree) is defined in XY-plane and hence X-component and Y-component for flow direction are taken as 0.929133 and 0.369747 respectively. The inlet boundary conditions for the turbulence variables are calculated by the turbulent intensity and hydraulic diameter which is the diameter of fuselage in this case. The operating pressure is nullified.

The gradient required for calculating the cell face values, diffusion terms, and velocity gradients

are computed by Green-Gauss node based evaluation as it more accurate than Green-Gauss cell based and least square based evaluation technique at the expense of relatively more computational effort. Second order implicit formulation is used for the transient term. The courant number is taken as 0.1 and under-relaxation factors for the transport variables are set as 0.5. Differentiable flux limiter with the cell-to-cell limiting is used for smooth field variable variation as the flow undergoes with the shock.

The convergence criteria is limit out to be based on residuals of continuity, momentum, energy and turbulence equations. It is set to be $1e^{-04}$ for inviscid and then deduced to $1e^{-03}$ for turbulence flow due to slow convergence of density based solver. The coefficient of rolling moment, coefficient of drag and coefficient of lift are monitored for each time step. Flow is initialized from inlet boundary condition values. The time step is described as 0.1 sec and the maximum iterations per time step are 400.

5.3 Nominal Case Results

The values of coefficients and contour plots are extracted and the normalized total pressure change contours are compared with the literature.

5.3.1 Values of Coefficients

The convergence of three coefficients against the time is plotted in the figure (5.4). The steady graphs for C_m , C_D and C_L from around 2 sec to 4.5 sec evident the convergence of inviscid flow solution. While reaching residual criteria for convergence, the coefficients appears to be converged and these converged values of the coefficients are reported in the table (5.1).

Since undefined geometrical parameter (\varkappa), the value of coefficient of rolling moment can not be compared with its value given by Khelil et al. [16] which is extracted from graph and approximately equal to 0.84.

These values of coefficients are considered for GSA and the percentage change over these values for all the cases of GSA are evaluated to compare their effect.

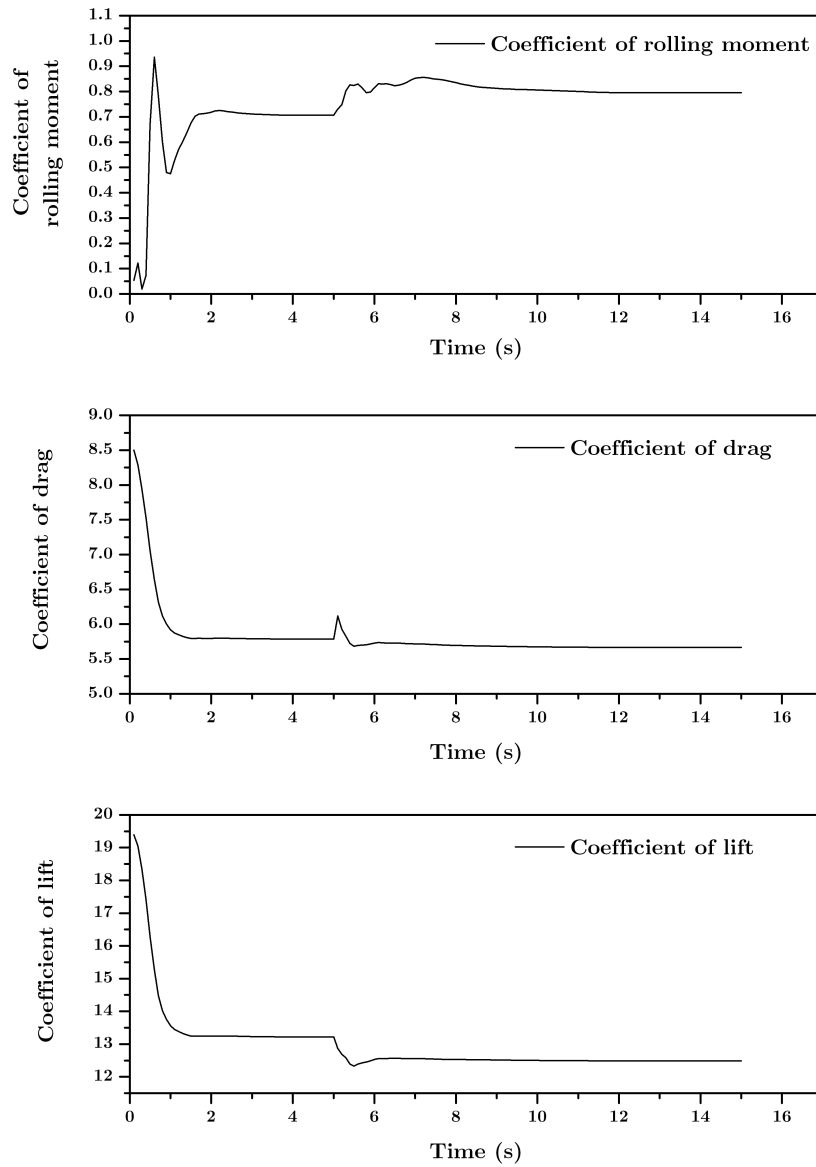


Figure 5.4: Convergence of C_m , C_D and C_L

Table 5.1: Nominal Case Result for Coefficients

Coefficients	Nominal Case Result
Coefficient of rolling moment (C_m)	0.79592939
Coefficient of drag (C_D)	5.666157
Coefficient of lift (C_L)	12.48928

5.3.2 Contour Plots

The contours of mach number are plotted for sections of missile. The figure (5.5) shows the mach number contours for the horizontal plane which is the plane $Y = 0$. The shock midway of the body is due to the presence of wing and same can be seen near tip region of the tail. The unsymmetrical

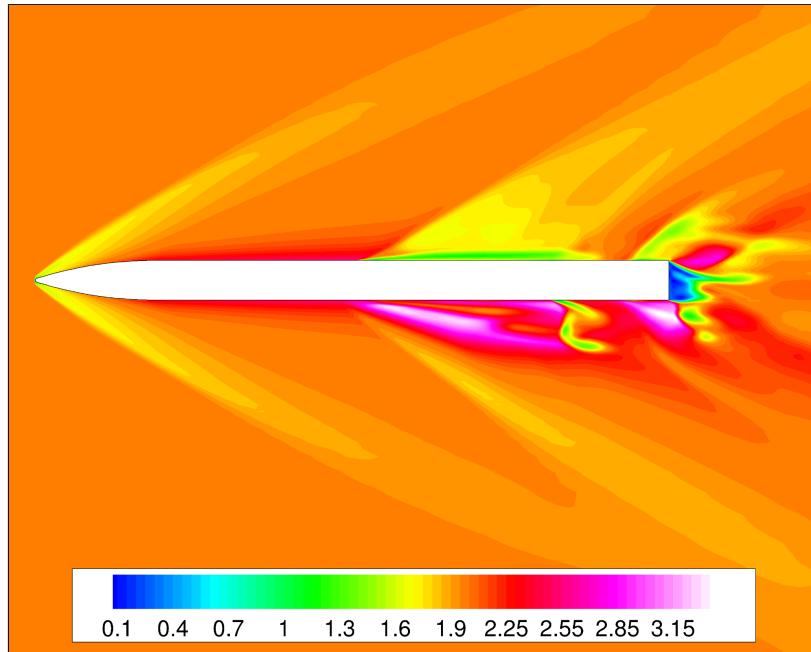


Figure 5.5: Mach Number Contours at Plane $Y = 0$

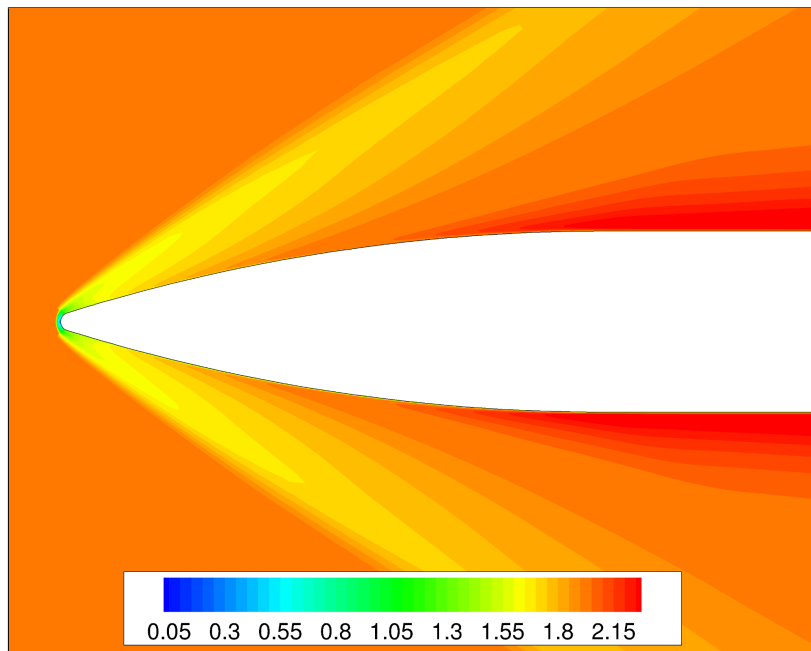


Figure 5.6: Prandtl-Meyer Expansion and Bow Shock at Plane $Y = 0$

contours about the axis and after the midway is caused by the existence of roll angle (ϕ) which is equal to 22.5 degree. The maximum mach number reached is about 3.2 while its minimum is around 0.1 in the region past the fuselage. The figure (5.6) exhibits the Prandtl-Meyer expansion after the nose section in the plane $Y = 0$ and it is evident from the steady upsurge in mach number which is to 2.2. The flow upstream to nose shows the bow shock.

The mach number contours for the vertical plane or plane $Z = 0$ is shown in figures (5.7) and (5.8). Here, the unsymmetrical mach contours are originated ahead of the wings region due to the angle of attack while both angle of attack and roll angle are responsible for unsymmetrical mach contours from the wings region. The mach number is reduced to about 0.05 from free-stream mach number of 2 after the bow shock ahead of nose.

The figure (5.9) presents the contours of normalized stagnation pressure change in the plane $Z = 0$ behind the fuselage base with velocity vectors. The normalized stagnation pressure is defined as the ratio of difference between free stream stagnation pressure ($P_{T\infty}$) and the local stagnation pressure (P_T) to the free stream stagnation pressure ($P_{T\infty}$) i.e. equal to $\left(\frac{P_{T\infty}-P_T}{P_{T\infty}}\right)$. The flow circulation associated with its reattachment are encountered zone next to the fuselage base. The decrease in pressure causes the flow to be recirculated region past the fuselage.

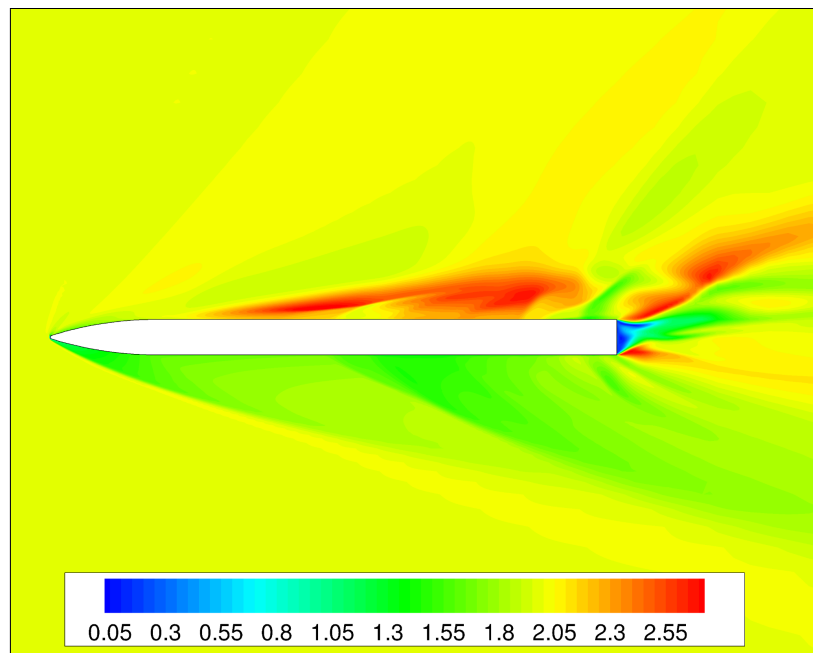


Figure 5.7: Mach Number Contours at Plane $Z = 0$

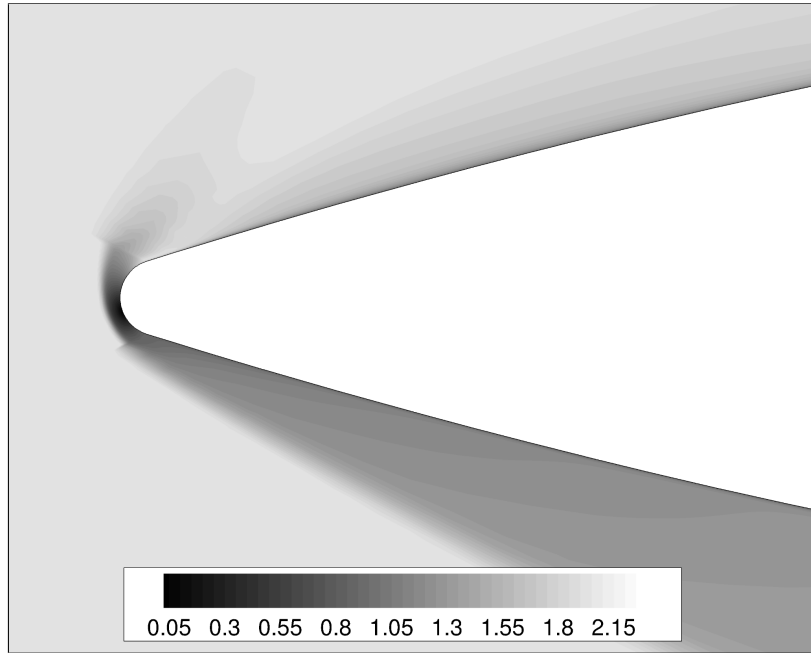


Figure 5.8: Bow Shock at Plane $Z = 0$

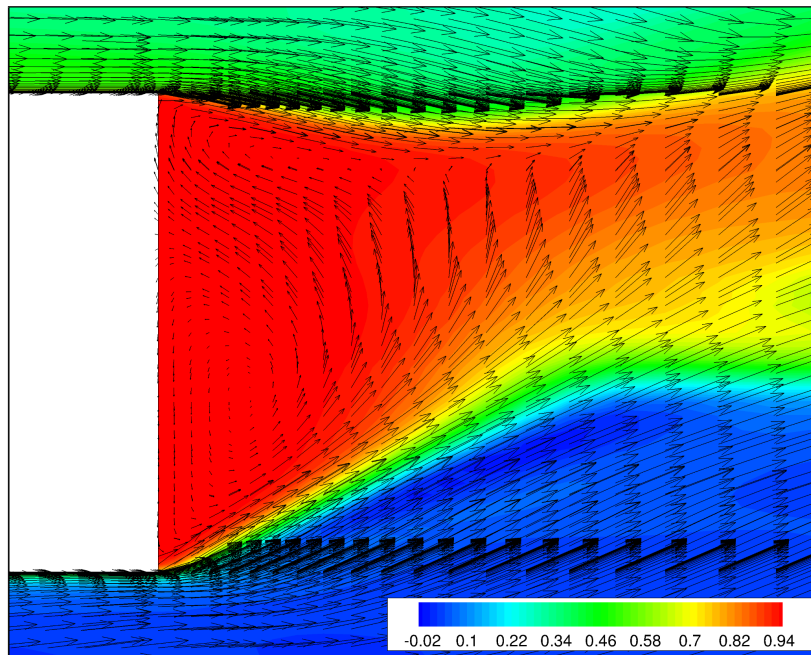


Figure 5.9: Circulation and Reattachment at Plane $Z = 0$

The vortices formed due to the presence of roll angle given can be observed from the stagnation pressure change. The figure (5.10) shows the contours of normalized stagnation pressure change for the different sections along the axis of the missile. The vortices evolution can be seen throughout the length of the missile. The symmetrical pattern of the contours up to the wings become antisymmetric when flow passes through the wings portion. The two vortices structure formed over fuselage

interacts with the vortices resulted due to wings and the severity of unsymmetrical vortices magnify in downstream flow passing the wings. This triggers the rolling moment about the central axis of the missile.

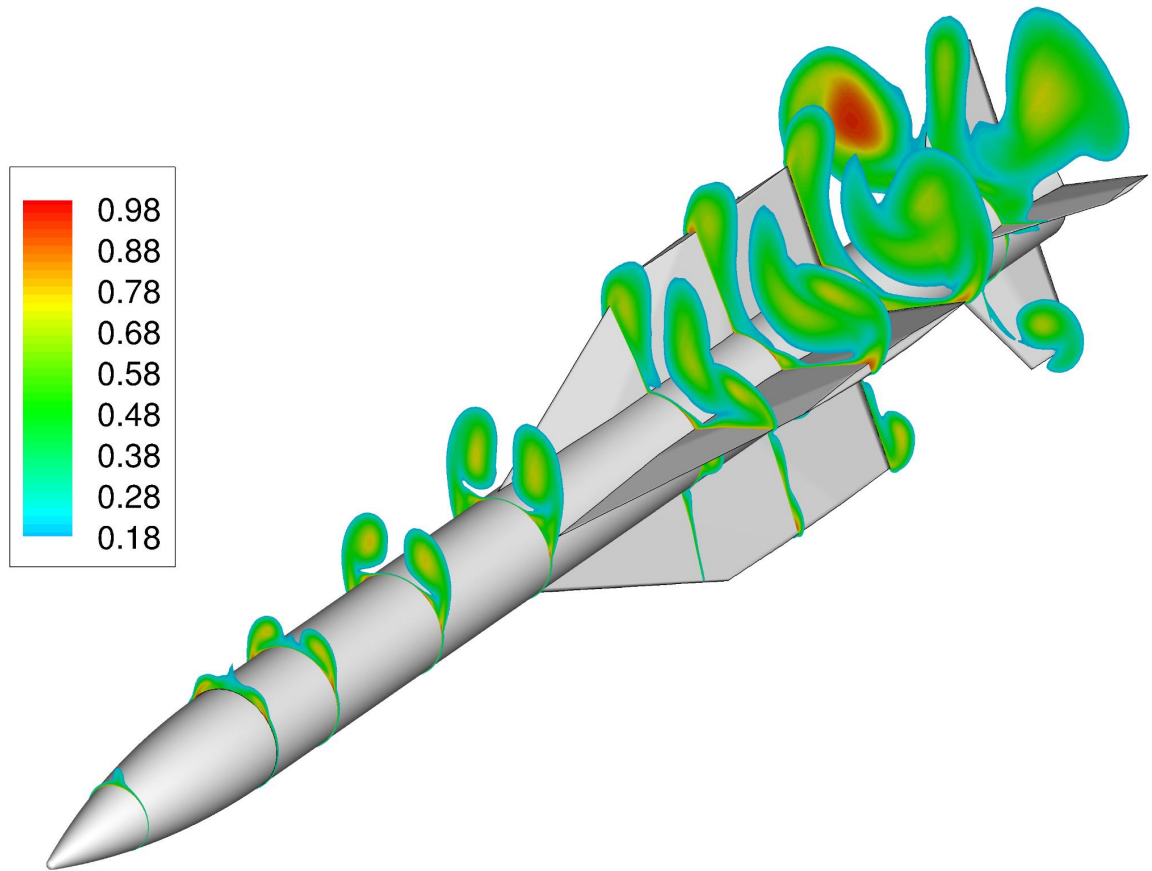
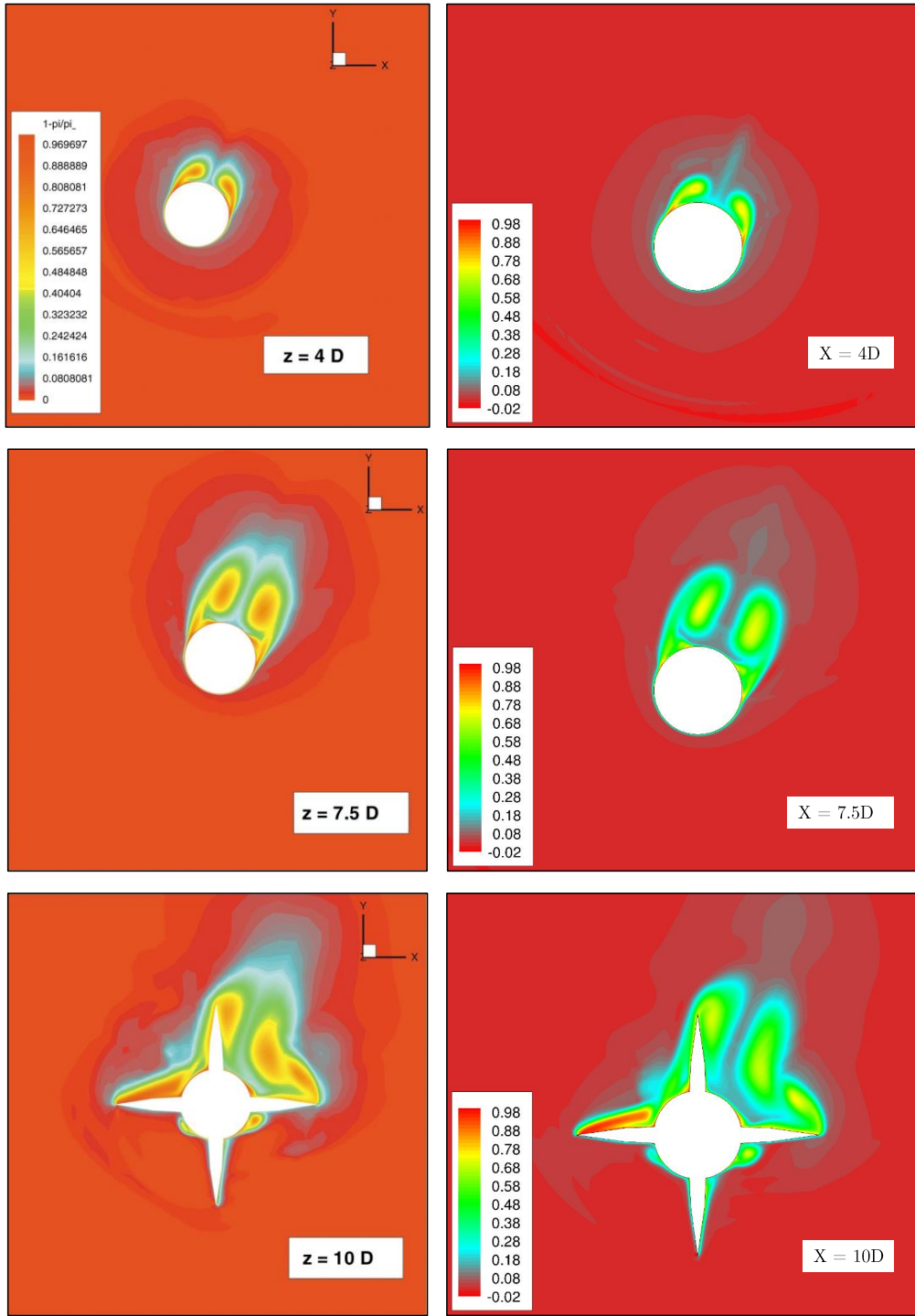


Figure 5.10: Sectional Contours Of Normalized Stagnation Pressure Change

5.3.3 Comparison of Contours

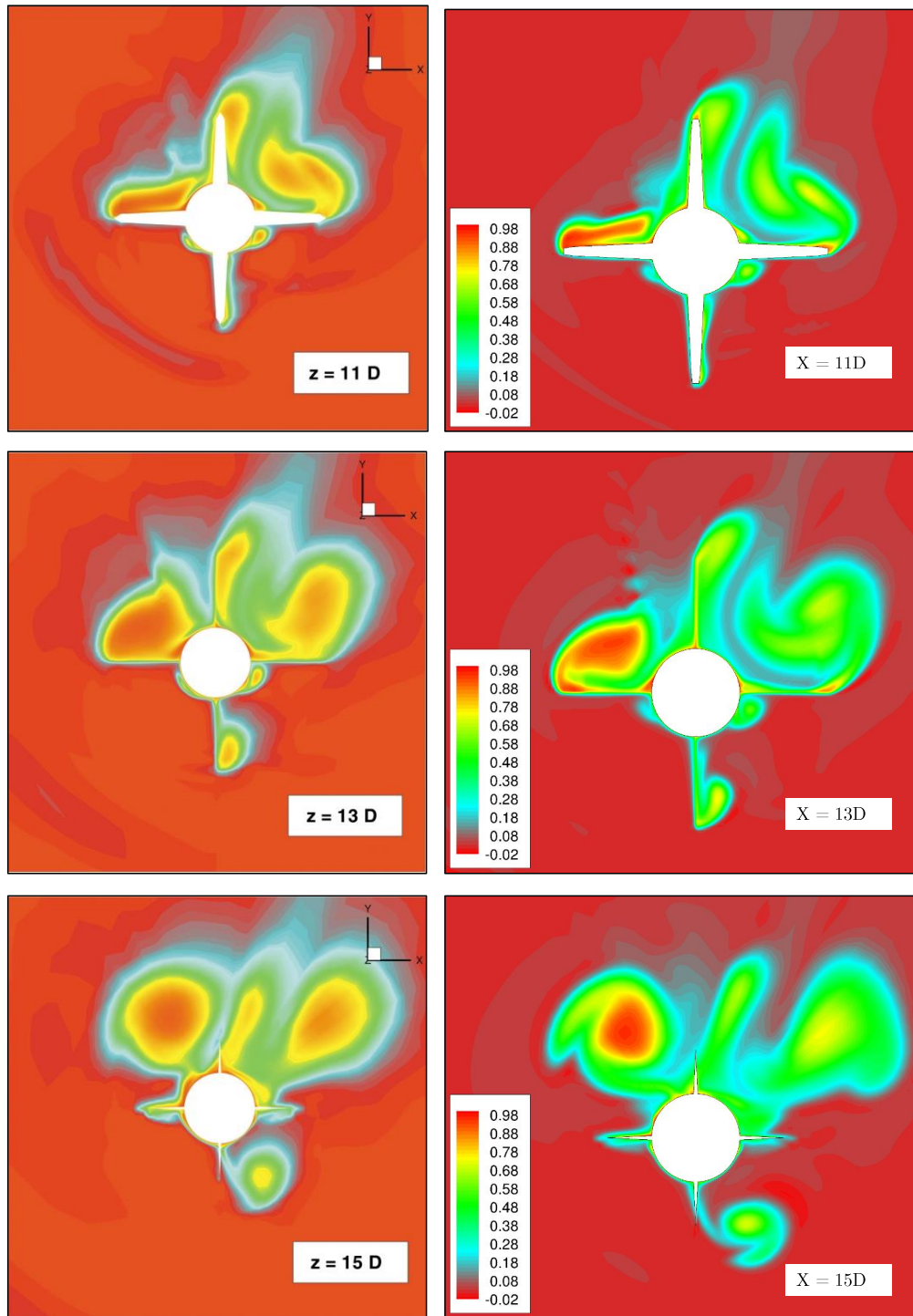
The figures (5.11) and (5.12) demonstrates the comparison of contours of stagnation pressure change $\left(= \frac{P_{T\infty} - P_T}{P_{T\infty}} \right)$ between Khelil et al. [16] and simulation results. The contours are plotted for the sections $X = 4D$, $7.5D$, $10D$, $11D$, $13D$, and $15D$. An appropriate similarity is found in the two results.



Khelil, et al., 2001

Simulations

Figure 5.11: Contours Comparison of Pressure Change at Planes $X = 4D$, $7.5D$, $10D$

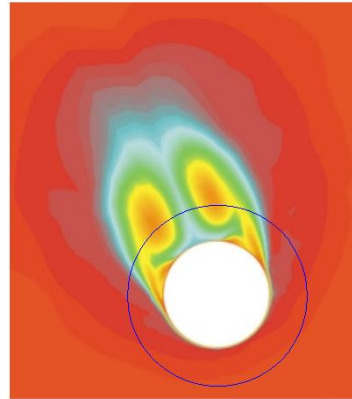


Khelil, et al., 2001

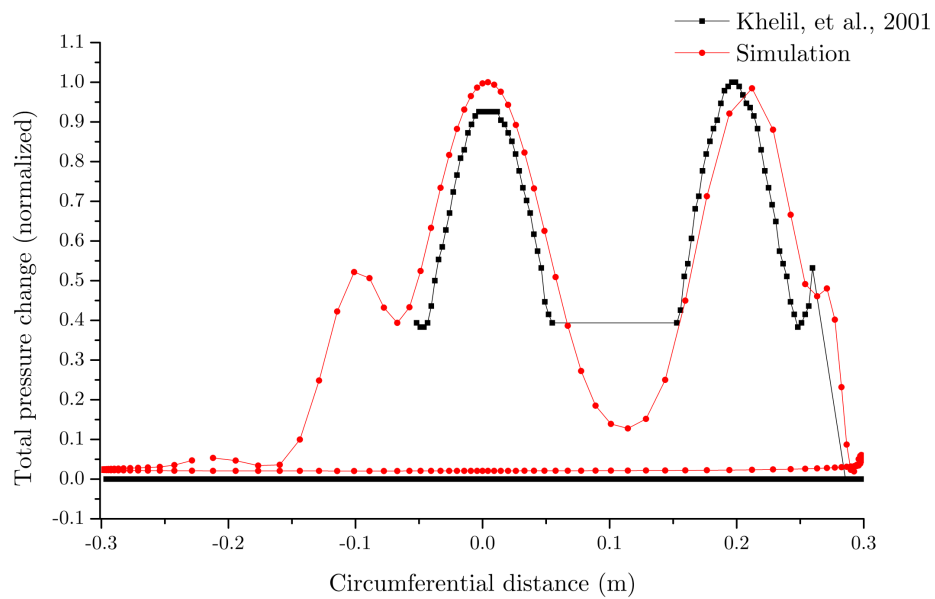
Simulations

Figure 5.12: Contours Comparison of Pressure Change at Planes $X = 11D$, $13D$, $15D$

A qualitative comparison between Khelil et al. [16] and simulation results is made in figure (5.13). The values of the normalized stagnation pressure change are extracted from the circumference of a circle of the radius equal to 30 cm and the cross-section considered here is $X = 7.5D$. The positions of peaks of pressure change are almost same for both the results.



(a)



(b)

Figure 5.13: Plot for Comparison of Pressure Change Contours at Plane $7.5D$ and $R = 30$ cm

Chapter 6

GCI And GSA Results

In this chapter, the results of grid convergence study and sensitivity analysis are presented. The strategy used for all simulations is identical to the nominal case in which inviscid solution is simulated followed by the turbulent flow.

6.1 GCI Results

The three grids required to calculate the Grid Convergence Index (GCI) are created. The number of intervals on each edge of the nominal case mesh is reduced by 30% and increased by 30% to generate the coarse mesh and finest mesh respectively. The advancement ratios of intervals are kept constant so that the consistency in three grids is preserved. The number of cells of generated meshes are 13.14, 5.32 and 2.58 million for the finest, fine and coarse grids respectively.

The refinement factors, r_{21} and r_{32} calculated from equations (4.6) are equal to 1.35 and 1.27 respectively. The factor of safety (F_S) taken here is equal to 1.25. The GCI over the fine grid is reported since it is practical to perform GSA simulations on the mesh of 5.32 million cells for the available computational facility.

6.1.1 GCI For Global Output Parameters

Coefficient of rolling moment (C_m), coefficient of drag (C_D) and coefficient of lift (C_L) are the prime targets of the problem and are considered for GCI calculations.

The table (6.1) shows the calculations of apparent order of accuracy (n), extrapolated values (ψ_{Ext}^{21}), conventional error (ξ_a^{21}), extrapolated error (ξ_{Ext}^{21}), and GCI over fine and finest grids for all the three coefficients. The coefficient of rolling moment undergoes the oscillatory convergence and coefficients of drag and lift shows monotonic convergence. The uncertainty due to the grid in the coefficient of rolling moment is 10.97% GCI for the fine grid while it is 5.20% for the finest mesh. The uncertainty in coefficients of drag and lift are 0.27% GCI and 0.66% GCI respectively for the fine grid while considering finest grid, they are of 0.10% GCI and 0.41% GCI. As expected, the GCI exhibits high uncertainty due to the grid in the case of fine mesh as compared to the finest mesh for all of the three coefficients. It can also be observed that coefficient of rolling moment is much more affected by the grid density as compared to lift and drag coefficients in this problem.

Table 6.1: GCI Estimation For Global Output Parameters

	Cell Count	C_m	C_D	C_L
Finest	13,146,260	0.76077806	5.658244	12.46448
Fine	5,316,960	0.79592939	5.666157	12.48928
Coarse	2,583,616	0.78087258	5.670096	12.5009
n		2.49	3.49	1.59
ψ_{Ext}^{21}		0.72914463	5.653967	12.423924
ξ_a^{21}		4.62%	0.14%	0.20%
ξ_{Ext}^{21}		4.33%	0.08%	0.33%
GCI_{fine}^{12}		10.97%	0.27%	0.66%
GCI_{finest}^{21}		5.20%	0.10%	0.41%

6.1.2 GCI For Local Field Variables

GCI is also estimated for the local field variables such as mach number (M) and normalized stagnation pressure change ($= \frac{P_{T\infty} - P_T}{P_{T\infty}}$). The local variables are calculated from area-weighted integration of the points along a line. Figure (6.1) shows the line from which values are extracted

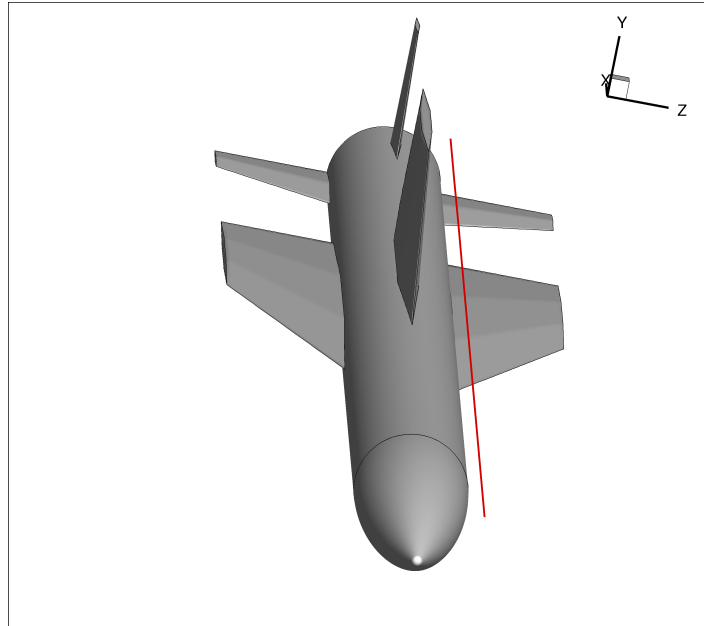


Figure 6.1: Line Drawn In Space To Evaluate Local GCI

and it is parallel to the axis of the missile. The points are twenty in number and placed equidistant except with last two points. The length of the line is equal to the length of missile ($= 16D$) with the end coordinates $(0, 0.175, 0.175)$ and $(5.6, 0.175, 0.175)$.

Table (6.2) shows the estimation of GCI on fine mesh for mach number. The apparent order of accuracy (n) for local variables is varying in a wide range and is also observed by Celik and Ozgur [13]. The maximum GCI spotted for mach number is 6.00%. Similarly, the table (6.3) gives the GCI estimation for normalized stagnation pressure change. Some points demonstrate a very high GCI for pressure change which might be because of the very low apparent order of accuracy.

Table 6.2: GCI For Local Mach Number Over A Specified Line

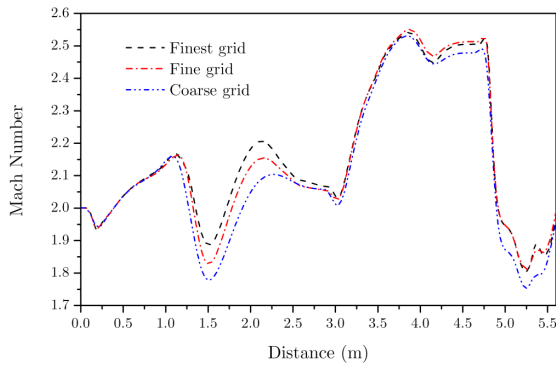
No.	Finest	Fine	Coarse	n	ψ_{Ext}^{21}	ξ_a^{21}	ξ_{Ext}^{21}	GCI_{fine}^{12}
1	1.999889	2.000156	2.001704	7.6498	1.99986	0.01	0.00	0.02
2	1.967092	1.976331	1.961994	1.672	1.952914	0.47	0.73	1.49
3	2.070796	2.071503	2.063391	10.0412	2.070759	0.03	0.00	0.04
4	2.127274	2.124633	2.123135	1.0219	2.134632	0.12	0.34	0.59
5	2.206263	2.205137	2.081235	19.692	2.206266	0.05	0.00	0.06
6	1.865779	1.815673	1.733212	2.73	1.905267	2.69	2.07	6.00
7	1.972659	1.945268	1.941259	5.0217	1.980455	1.39	0.39	2.23
8	2.12656	2.086018	2.100462	3.0141	2.154124	1.91	1.28	4.00
9	2.079709	2.060795	2.107191	3.5033	2.08987	0.91	0.49	1.75
10	2.053664	2.040434	2.080472	4.3694	2.058545	0.64	0.24	1.10
11	2.035528	2.031327	2.048524	5.6366	2.036477	0.21	0.05	0.32
12	2.313499	2.321442	2.26486	8.001	2.312708	0.34	0.03	0.47
13	2.499948	2.512915	2.439864	6.996	2.498137	0.52	0.07	0.74
14	2.560414	2.567085	2.506833	9.0192	2.559936	0.26	0.02	0.35
15	2.460558	2.474072	2.426959	4.9608	2.45662	0.55	0.16	0.89
16	2.527822	2.534562	2.447757	10.5418	2.527525	0.27	0.01	0.35
17	2.526266	2.488429	2.332952	6.2786	2.533045	1.50	0.27	2.21
18	1.915609	1.913304	1.810654	15.9418	1.915628	0.12	0.00	0.15
19	1.865643	1.855769	1.761455	9.6432	1.866221	0.53	0.03	0.70
20	1.984203	1.977848	1.929111	8.7601	1.984697	0.32	0.02	0.43

Table 6.3: GCI For Local Pressure Change Over A Specified Line

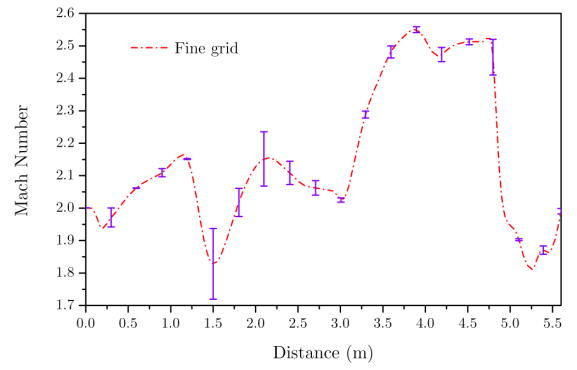
No.	Finest	Fine	Coarse	n	ψ_{Ext}^{21}	ξ_a^{21}	ξ_{Ext}^{21}	GCI_{fine}^{12}
1	0.000238	0.000177681	0.000028	4.2774	0.0003	25.49	8.90	44.08
2	0.002703	0.003248155	0.002078	2.9591	0.0023	20.17	16.41	42.83
3	0.035199	0.035916567	0.033226	5.2640	0.0350	2.04	0.53	3.21
4	0.095152	0.097113431	0.089385	5.4751	0.0947	2.06	0.50	3.20
5	0.165227	0.17198628	0.399142	14.7790	0.1651	4.09	0.05	5.18
6	0.732097	0.74644357	0.758151	0.0901	0.2086	1.96	250.89	91.83
7	0.717038	0.72480458	0.685941	6.4900	0.7157	1.08	0.18	1.58
8	0.620304	0.64278495	0.585991	3.6239	0.6089	3.62	1.88	6.83
9	0.564596	0.58901465	0.530271	3.4237	0.5510	4.33	2.47	8.42
10	0.495129	0.52085412	0.489796	0.7066	0.3862	5.20	28.20	33.99
11	0.429632	0.45377898	0.428023	0.2402	0.1066	5.62	303.08	101.01
12	0.27113	0.28120351	0.244812	5.1100	0.2684	3.72	1.03	5.92
13	0.182811	0.19114447	0.174375	2.7010	0.1761	4.56	3.79	10.26
14	0.155952	0.15890867	0.162562	1.6438	0.1513	1.90	3.06	6.09
15	0.135226	0.13948882	0.187923	10.3447	0.1350	3.15	0.15	4.13
16	0.140807	0.14770043	0.197656	8.5333	0.1402	4.90	0.41	6.63
17	0.173587	0.1873033	0.208655	2.5181	0.1614	7.90	7.52	18.63
18	0.187377	0.18214703	0.280942	12.1796	0.1875	2.79	0.07	3.58
19	0.229751	0.21979374	0.29261	8.1140	0.2307	4.33	0.41	5.94
20	0.237745	0.22415	0.274568	5.2206	0.2413	5.72	1.49	9.03

The values of mach number for three grids and GCI over the fine mesh are plotted in the figure (6.2). Similarly, the pressure change values and GCI are plotted in the figure (6.3). A shaded plot is shown in figure (6.2) gives region for the uncertainty region due to the grid. The shaded plot could not be shown for pressure change since some of the points are having wide range of uncertainty and hence are skipped.

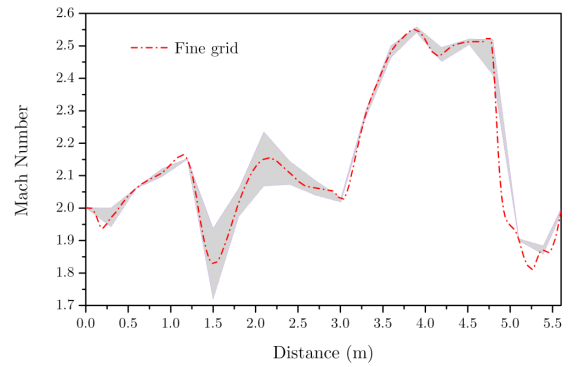
The points corresponding to disperse plots or the large difference between the values of three grids are having larger GCI than those with a small difference.



(a) Values For Three Grids

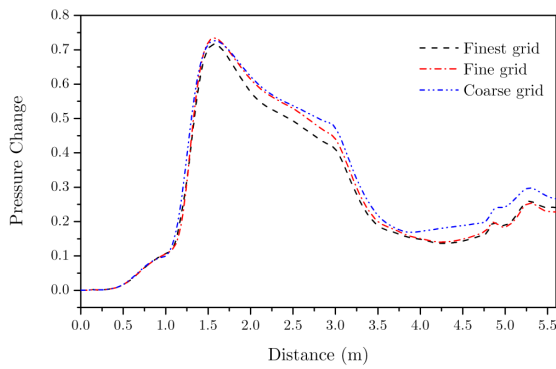


(b) GCI Over Fine Grid Represented By Bars

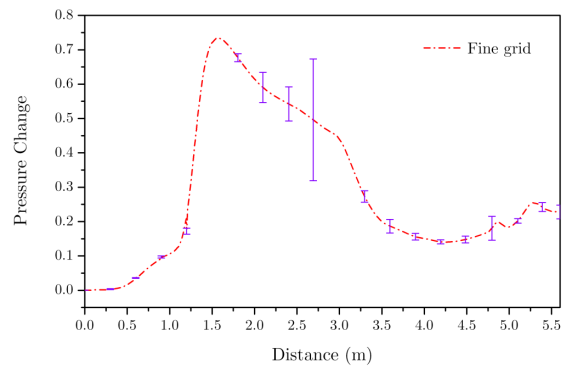


(c) GCI Over Fine Grid Represented By Shaded Region

Figure 6.2: Local GCI Evaluation For Mach Number On Specified Line



(a) Values For Three Grids



(b) GCI Over Fine Grid Represented By Bars

Figure 6.3: Local GCI Evaluation For Normalized Stagnation Pressure Change On Specified Line

GCI calculated for points can also be used to identify the regions where the grid refinement is required and this approach is successfully used by Ching-Fang et al. [36].

6.2 GSA Results

After GCI study, the simulations are performed for Global Sensitivity Analysis (GSA) on the fine mesh. Table (6.4) shows the effectiveness of perturbations of nine input parameters on the global output variables (C_m , C_D , and C_L).

Table 6.4: GSA Results

Parameter	Perturbations	C_m	C_D	C_L
Geometrical Parameter (\varkappa)	21D/3	0.83268369	5.648708	12.44292
	25D/3	0.79442892	5.753036	12.64808
Turbulence Model	Standard $k - \omega$	0.87426188	5.859763	12.76505
	SST $k - \omega$	0.78237749	5.64544	12.51797
Viscosity Model	Kinetic Theory	0.79580182	5.666393	12.48912
	Power Law	0.79561599	5.666621	12.48872
Thermal Conductivity	Kinetic Theory	0.79585377	5.666196	12.48935
	Polynomial	0.79586964	5.666114	12.48917
Specific Heat	Kinetic Theory	0.7972854	5.66943	12.49683
	Piecewise Polynomial	0.79469752	5.6594	12.47386
Static Temperature	166.67–3.96 K	0.79582206	5.665207	12.49014
	166.67+3.96 K	0.79395001	5.665918	12.48679
Turbulence Intensity	0.5%	0.79081323	5.658112	12.4777
	1.5%	0.79435294	5.67198	12.49798
Flux Type	Roe–FDS	0.77002	5.65645	12.45026
Discretization Scheme Order	1 st Order	0.68164467	5.988331	13.12935
	3 rd Order	0.76662402	5.687919	12.51823

The output values obtained from perturbations are compared for GSA on the basis of absolute percentage change from the corresponding nominal case output value. Figures (6.4), (6.5) and (6.6) illustrates the plots for percentage change for coefficient of rolling moment, drag coefficient and lift coefficient.

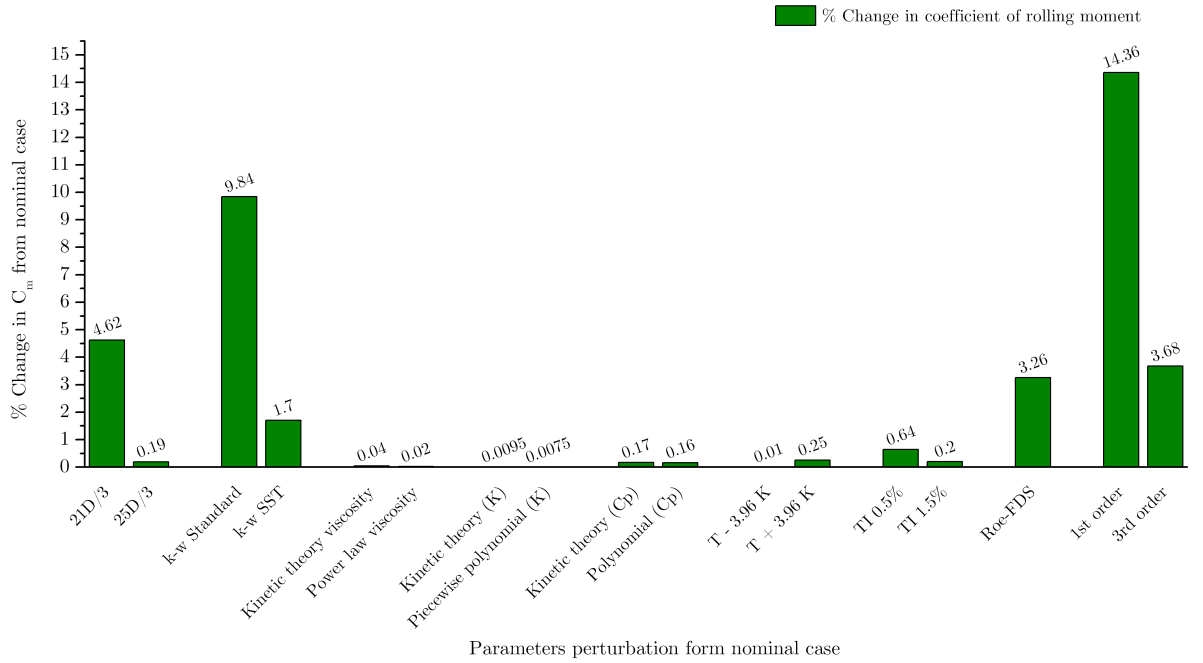


Figure 6.4: GSA For C_m

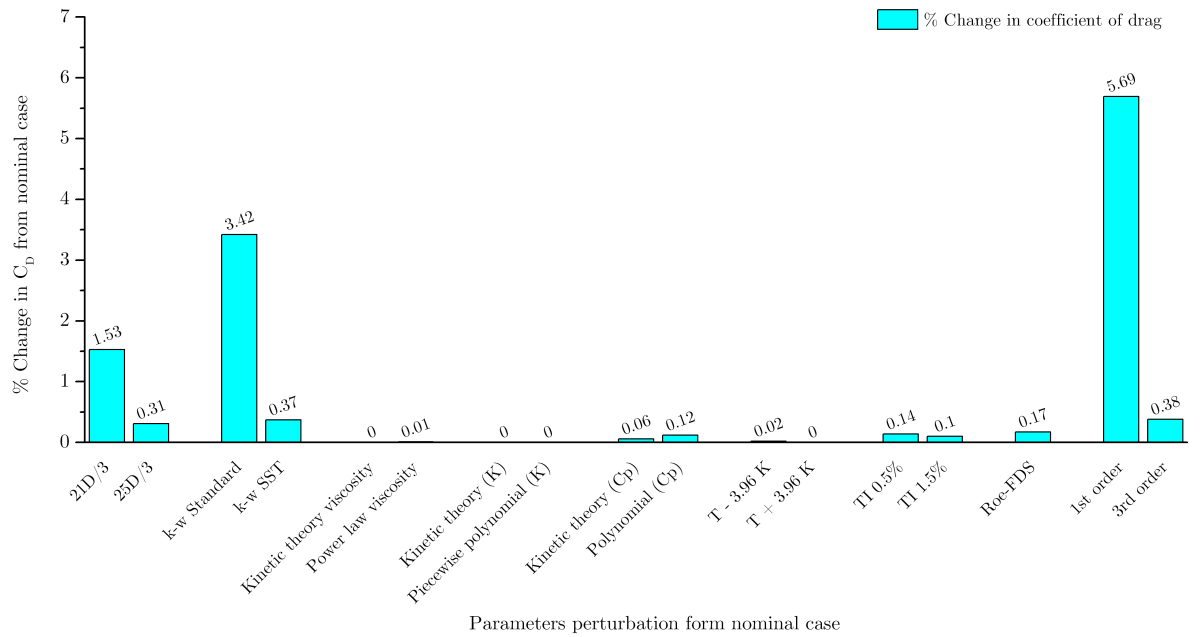


Figure 6.5: GSA For C_D

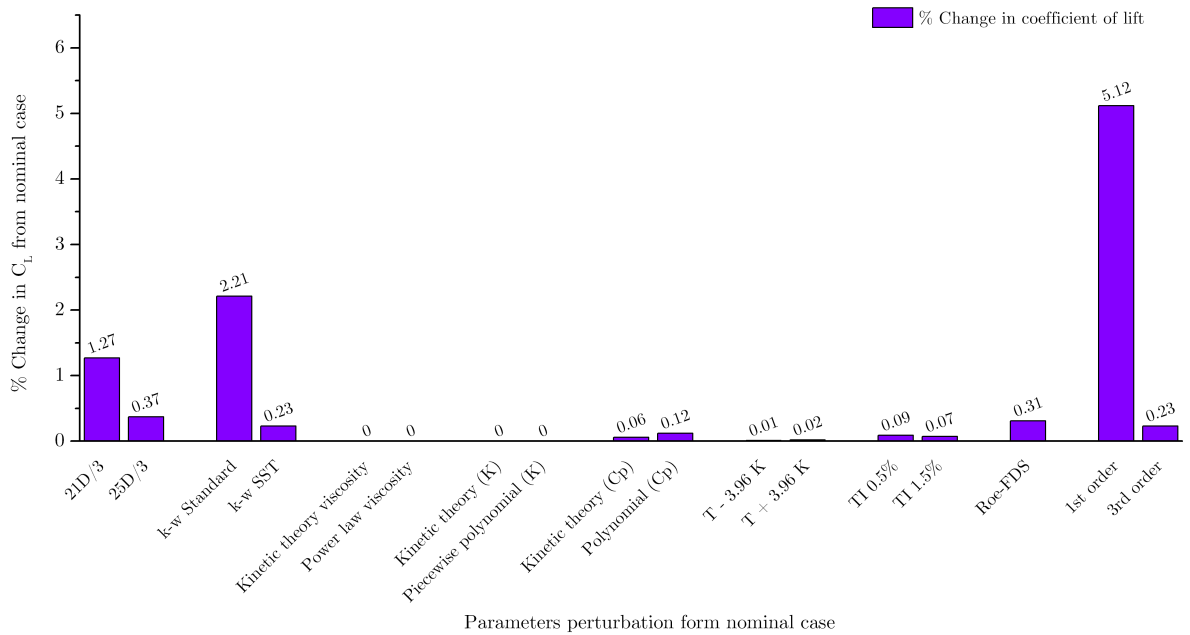


Figure 6.6: GSA For C_L

The figure (6.4) shows that C_m is affected by geometrical uncertainty, turbulence model, inviscid flux type and order of discretization scheme constituting more than 1% difference from the nominal value. Other input parameters including the viscosity, thermal conductivity, specific heat modellings, turbulent intensity and temperature uncertainty contribute less for altering the coefficients. The same trends are observed for C_D and C_L .

It is also evident from the charts that $k - \omega$ models also disagree with Spalart-Allmaras model though both are considered to be an adequate approximation for the aerospace applications or external wall-bounded flows with the adverse pressure gradient. Turbulence intensity has about 0.64% change in C_m from the nominal value. As expected, coefficient values from the first order scheme deviate from the nominal case values more. But the third order scheme is also seen to more effective which is about 3.68% in the investigation of C_m .

Chapter 7

Conclusions and Future Scope

A systematic methodology is propounded for Grid Convergence Index (GCI) and Global Sensitivity Analysis (GSA).

Uncertainty due to the grid is quantified by using GCI. It is reliable to use GCI for reporting the grid uncertainty for the practical problems where the computational power is limited. Here GCI has been defined on 5.3 million cell mesh as it is computationally affordable to use. GCI for global output quantities C_m , C_D and C_L are 10.97%, 0.27% and 0.66% respectively. GCI can also be used to estimate the grid sensitivity on local field variables. Thus, GCI is constructive to recognize the mesh that should be used by giving its error.

GSA is used to identify the input parameters leading the effect on output result. Geometrical uncertainty, turbulence models, inviscid flux type and the order of discretization scheme have a substantial influence on the global output parameters which is more than 1% of nominal case values. Turbulent intensity also constitutes a small but considerable influence. Effect of physical properties modelling can be securely ignored as the solution is unaltered.

These influential input parameters can be scrutinized for detailed uncertainty estimation for future work. The interdependency of these uncertain input parameters can be significant in the worst case scenario and is essential to examine for reporting the uncertainty. A separate study can be done in which GCI can be used to control localized grid to improve the solution.

References

- [1] W. L. Oberkampf, J. C. Helton, and K. Sentz, “Mathematical representation of uncertainty,” in *AIAA Non-Deterministic Approaches Forum*, no. 2001-1645, pp. 16–19, 2001.
- [2] D. Frostbutter, B. E. McGrath, and R. P. Rog er, “Application of computational fluid dynamics in missile engineering,” *Johns Hopkins APL Technical Digest*, vol. 22, no. 3, pp. 289–301, 2001.
- [3] G. Agbaglah, S. Delaux, D. Fuster, J. Hoepffner, C. Josserand, S. Popinet, P. Ray, R. Scardovelli, and S. Zaleski, “Parallel simulation of multiphase flows using octree adaptivity and the volume-of-fluid method,” *Comptes Rendus Mecanique*, vol. 339, no. 2, pp. 194–207, 2011.
- [4] ASME, “V&V 10-2006: guide for verification and validation in computational solid mechanics,” *New York: American Society of Mechanical Engineers (ASME)*, 2006.
- [5] F. Stern, R. V. Wilson, H. W. Coleman, E. G. Paterson, *et al.*, “Verification and validation of cfd simulations,” *Iowa Institute of Hydraulic Research, The University of Iowa, IIHR Report*, no. 407, 1999.
- [6]  . Turgeon, D. Pelletier, and J. Borggaard, “Applications of continuous sensitivity equations to flows with temperature-dependent properties,” *Numerical Heat Transfer: Part A: Applications*, vol. 44, no. 6, pp. 611–624, 2003.
- [7]  . Turgeon, D. Pelletier, and J. Borggaard, “Application of a sensitivity equation method to the k - ϵ model of turbulence,” in *Fifteenth AIAA Computational Fluid Dynamics Conference, AIAA Paper 2001*, vol. 2534, 2001.
- [8] A. G. Godfrey and E. M. Cliff, “Sensitivity equations for turbulent flows,” in *AIAA, Aerospace Sciences Meeting and Exhibit, 39th, Reno, NV*, 2001.
- [9] X. Du and W. Chen, “Methodology for managing the effect of uncertainty in simulation-based design,” *AIAA journal*, vol. 38, no. 8, pp. 1471–1478, 2000.
- [10] Y. Pei, R. Shan, S. Som, T. Lu, D. Longman, and M. J. Davis, “Global sensitivity analysis of a diesel engine simulation with multi-target functions,” tech. rep., SAE Technical Paper, 2014.
- [11] M. N. Rhode and W. L. Oberkampf, “Estimation of uncertainties for a supersonic retro-propulsion model validation experiment in a wind tunnel,” *AIAA Paper*, vol. 2707, 2012.
- [12] I. B. Celik, U. Ghia, P. J. Roache, *et al.*, “Procedure for estimation and reporting of uncertainty due to discretization in {CFD} applications,” *Journal of fluids {Engineering-Transactions} of the {ASME}*, vol. 130, no. 7, 2008.

- [13] I. Celik and O. Karatekin, “Numerical experiments on application of Richardson extrapolation with nonuniform grids,” *Journal of fluids engineering*, vol. 119, no. 3, pp. 584–590, 1997.
- [14] L. Eça and M. Hoekstra, “A procedure for the estimation of the numerical uncertainty of CFD calculations based on grid refinement studies,” *Journal of Computational Physics*, vol. 262, pp. 104–130, 2014.
- [15] K. S. Abdol-Hamid and F. Ghaffari, “Error estimate of the Ares I vehicle longitudinal aerodynamic characteristics based on turbulent navier-stokes analysis,” *AIAA Paper*, vol. 3646, p. 2011, 2011.
- [16] S. B. Khelil, P. Guillen, M. Lazareff, and R. G. Lacau, “Numerical simulation of roll induced moment of cruciform tactical missiles,” *Aerospace science and technology*, vol. 5, no. 2, pp. 109–124, 2001.
- [17] P. R. Spalart and S. R. Allmaras, “A one equation turbulence model for aerodynamic flows.,” *AIAA journal*, vol. 94, 1992.
- [18] S. Deck, P. Duveau, P. d’Espiney, and P. Guillen, “Development and application of Spalart–Allmaras one equation turbulence model to three-dimensional supersonic complex configurations,” *Aerospace Science and Technology*, vol. 6, no. 3, pp. 171–183, 2002.
- [19] N. Kumar and M. T. Nair, “Application of density corrected Spalart–Allmaras model to flow past ogive cylinder at high angles of attack,” *Journal of Applied Fluid Mechanics*, vol. 6, no. 3, pp. 375–384, 2013.
- [20] D. C. Wilcox, “Reassessment of the scale-determining equation for advanced turbulence models,” *AIAA journal*, vol. 26, no. 11, pp. 1299–1310, 1988.
- [21] F. R. Menter, “Two-equation eddy-viscosity turbulence models for engineering applications,” *AIAA journal*, vol. 32, no. 8, pp. 1598–1605, 1994.
- [22] M. Coussirat, A. Guardo, E. Jou, E. Egusquiza, E. Cuerva, and P. Alavedra, “Performance and influence of numerical sub-models on the CFD simulation of free and forced convection in double-glazed ventilated façades,” *Energy and Buildings*, vol. 40, no. 10, pp. 1781–1789, 2008.
- [23] B. Launder, G. J. Reece, and W. Rodi, “Progress in the development of a Reynolds-stress turbulence closure,” *Journal of fluid mechanics*, vol. 68, no. 03, pp. 537–566, 1975.
- [24] S.-w. Li, S. Wang, J.-p. Wang, and J.-c. Mi, “Effect of turbulence intensity on airfoil flow: numerical simulations and experimental measurements,” *Applied Mathematics and Mechanics*, vol. 32, pp. 1029–1038, 2011.
- [25] O. Redlich and J. N. Kwong, “On the thermodynamics of solutions. v. an equation of state. Fugacities of gaseous solutions.,” *Chemical reviews*, vol. 44, no. 1, pp. 233–244, 1949.
- [26] D.-Y. Peng and D. B. Robinson, “A new two-constant equation of state,” *Industrial & Engineering Chemistry Fundamentals*, vol. 15, no. 1, pp. 59–64, 1976.
- [27] W. Sutherland, “LII. the viscosity of gases and molecular force,” *The London, Edinburgh, and Dublin Philosophical Magazine and Journal of Science*, vol. 36, no. 223, pp. 507–531, 1893.

- [28] K. Stephan and A. Laesecke, “The thermal conductivity of fluid air,” *Journal of physical and chemical reference data*, vol. 14, no. 1, pp. 227–234, 1985.
- [29] P. Roe, “Characteristic-based schemes for the Euler equations,” *Annual review of fluid mechanics*, vol. 18, no. 1, pp. 337–365, 1986.
- [30] M.-S. Liou and C. J. Steffen, “A new flux splitting scheme,” *Journal of Computational physics*, vol. 107, no. 1, pp. 23–39, 1993.
- [31] J. H. Lee and O. H. Rho, “Numerical analysis of hypersonic viscous flow around a blunt body using Roe’s FDS and AUSM+ schemes,” *AIAA paper*, pp. 97–2054, 1997.
- [32] W. K. Anderson, J. L. Thomas, and B. Van Leer, “Comparison of finite volume flux vector splittings for the euler equations,” *AIAA journal*, vol. 24, no. 9, pp. 1453–1460, 1986.
- [33] L. F. Richardson, “The approximate arithmetical solution by finite differences of physical problems involving differential equations, with an application to the stresses in a masonry dam,” *Philosophical Transactions of the Royal Society of London. Series A, Containing Papers of a Mathematical or Physical Character*, vol. 210, pp. 307–357, 1911.
- [34] P. J. Roache, “Perspective: a method for uniform reporting of grid refinement studies,” *Journal of Fluids Engineering*, vol. 116, no. 3, pp. 405–413, 1994.
- [35] P. J. Roache, “Quantification of uncertainty in computational fluid dynamics,” *Annual review of fluid Mechanics*, vol. 29, no. 1, pp. 123–160, 1997.
- [36] C.-F. A. Chen, R. D. Lotz, and B. E. Thompson, “Assessment of numerical uncertainty around shocks and corners on blunt trailing-edge supercritical airfoils,” *Computers & fluids*, vol. 31, no. 1, pp. 25–40, 2002.
- [37] S. R. Allmaras and F. T. Johnson, “Modifications and clarifications for the implementation of the Spalart-Allmaras turbulence model,” in *Seventh International Conference on Computational Fluid Dynamics (ICCFD7)*, pp. 1–11, 2012.
- [38] D. C. Wilcox, “Formulation of the k - ω turbulence model revisited,” *AIAA journal*, vol. 46, no. 11, pp. 2823–2838, 2008.
- [39] F. Menter, M. Kuntz, and R. Langtry, “Ten years of industrial experience with the SST turbulence model,” *Turbulence, heat and mass transfer*, vol. 4, no. 1, pp. 625–632, 2003.
- [40] S. Chapman and T. G. Cowling, *The mathematical theory of non-uniform gases: an account of the kinetic theory of viscosity, thermal conduction and diffusion in gases*. Cambridge university press, 1970.